

City Research Online

City, University of London Institutional Repository

Citation: Fu, F., Xiang, W., Qian, K. & Liu, W. (2026). Study on Failure Mechanism and Dynamic Response of RC Shear Wall in Tall Buildings under Impact Load. Journal of Structural Engineering, 152(1), 04025226. doi: 10.1061/jsendh.steng-15096

This is the accepted version of the paper.

This version of the publication may differ from the final published version.

Permanent repository link: https://openaccess.city.ac.uk/id/eprint/36172/

Link to published version: https://doi.org/10.1061/jsendh.steng-15096

Copyright: City Research Online aims to make research outputs of City, University of London available to a wider audience. Copyright and Moral Rights remain with the author(s) and/or copyright holders. URLs from City Research Online may be freely distributed and linked to.

Reuse: Copies of full items can be used for personal research or study, educational, or not-for-profit purposes without prior permission or charge. Provided that the authors, title and full bibliographic details are credited, a hyperlink and/or URL is given for the original metadata page and the content is not changed in any way.

City Research Online: http://openaccess.city.ac.uk/ publications@city.ac.uk/

Study on Failure Mechanism and Dynamic Response of RC Shear Wall in tall buildings under Impact Load

Feng Fu¹ F. ASCE, Weidong Xiang², Kai Qian³ M.ASCE, Wangxiang Liu⁴ Corresponding author Feng.fu.1@city.ac.uk¹ Qiankai@glut.edu.cn

Abstract: Currently, there are few studies on the impact resistance of RC shear walls in tall buildings. To this end, the dynamic response and failure mode of RC shear wall under impact load were investigated experimentally and numerically. 6 specimens were tested using a specialized pendulum impact rig. The parametric study was conducted to reveal the effects of wall height, impact position, reinforcement ratio, drop height and energy consumption. Based on the experimental results, an analytical model is established to predict the maximum displacement under impact load. Furthermore, more parameters were quantified by the verified numerical model using LS-DYNA. The obtained results show that the drop height and reinforcement ratio have a significant effect on the peak impact force. When the impact energy is constant, the energy absorption performance of the specimen is negatively correlated to the overall wall stiffness. The parametric results of LS-DYNA show that an increment of the axial compression ratio and wall width will significantly reduce the maximum displacement at the center of the wall. When the impact energy is low, increasing the impact velocity has a more significant effect on the displacement difference than the impact mass

Keywords: Pendulum impact test; Dynamic response; Numerical simulation, Drop height

Introduction

With the frequent occurrence of terrorist activities, industrial accidents, and natural disasters, reinforced concrete walls in tall buildings may suffer from the impact loads, especially for explosions (Do, T. V., Pham, T. M., and Hao, H. 2019. Impact force profile and failure classification of reinforced concrete bridge columns against vehicle impact. *Engineering Structures*, *183*, 443-458.Consolazio, G. R., and Cowan, D. R. 2005. Numerically efficient dynamic analysis of barge collisions with bridge piers. *Journal of Structural Engineering*, *131*(8), 1256-1266.), which will cause greater property losses and casualty. Typical examples include Murrah federal building explosion in 1995 and the 2015 Tianjin blast accident. As an integral part of

¹ Associate Professor, Dept. of Civil Engineering, School of Mathematics, Computer Science & Engineering, City, Univ. of London, Northampton Square, London EC1V 0HB, UK (corresponding author). Email: feng.fu.1@city.ac.uk ORCID: https:// orcid.org/0000-0002-9176-8159.

²Master's Candidate, College of Civil Engineering, Guilin Univ. of Technology, Guilin 541004, China. Email: 2120230918@glut.edu.cn
³Professor, College of Civil Engineering, Guilin Univ. of Technology, Guilin 541004, China. (corresponding author) Email: Qiankai@glut.edu.cn

⁴Engineer, KWEICHOE MOUTAI CO.LTD, GuiZhou, China. Email: <u>957360100@qq.com</u>

the building, research on the impact resistance of shear walls has become a crucial topic in the field of civil engineering. However, few researchers contributed their academic efforts to the dynamic response of shear walls under impact load.

29

30

31

32

33

34

35

36

37

38

39

40

41

42

43

44

45

46

47

48

49

50

51

52

53

54

55

56

57

58

59

In recent years, numerous scholars have investigated the dynamic response of various components under impact loading. The dynamic response analysis of a reinforced concrete (RC) beam is carried out using an impact test and model verification (Fujikake, K., Li, B., and Soeun, S. 2009. Impact response of reinforced concrete beam and its analytical evaluation. Journal of Structural Engineering, 135(8), 938-950. Fujikake, K. 2014. Impact performance of ultra-high-performance fiber reinforced concrete beam and its analytical evaluation. International Journal of Protective Structures, 5(2), 167-186.). Li et al. (Li, H., Chen, W., and Hao, H. 2020. Factors influencing impact force profile and measurement accuracy in drop weight impact tests. International Journal of Impact Engineering, 145, 103688.) believed that the primary impact peak is dominated by the impact energy and local contact stiffness, while the remaining part of the impact force is related to the mass ratio, contact stiffness, and flexural stiffness of the beam. Adhikary et al. (Adhikary, S. D., Li, B., and Fujikake, K. 2015, Residual resistance of impact-damaged reinforced concrete beams. Magazine of Concrete Research, 67(7), 364-378.) showed that the reinforcement ratio has a significant effect on the failure mode of RC beams under different loading rates. Guo et al. (Guo, J., Cai, J., and Chen, W. 2017. Inertial effect on RC beam subjected to impact loads. International Journal of Structural Stability and Dynamics, 17(04), 1750053.) obtained the relationship between peak load and peak torque. Li et al. (Li, H., Chen, W., Pham, T. M., and Hao, H. 2021. Analytical and numerical studies on impact force profile of RC beam under drop weight impact. International Journal of Impact Engineering, 147, 103743.) considered that the boundary conditions and concrete strength will significantly affect the maximum deflection and failure mode of RC beams. Xu et al. (Xu, B., and Zeng, X. 2014. Experimental study on the behaviors of reinforced concrete beams under impact loadings. China Civil Engineering Journal, 47(2), 41-51. (in chinese)) considered that the impact velocity, impact mass and reinforcement ratio greatly influence on the failure mode and dynamic response of RC beams. Some scholars have developed models to study the dynamic response of RC beams (Wang, W., Zhou, R.X. and Zhong, J. 2022. Efficient numerical analyses of RC beams subjected to impact loading using axial-flexure-shear fiber beam model. Structures, 41, 1559-1569.), but these models are only applicable to planar structures (Guner, S., and Vecchio, F. J. 2012. Simplified method for nonlinear dynamic analysis of shear-critical frames. ACI Structural Journal, 109(5), 727. Consolazio, G. R., and Davidson, M. T. 2008. Simplified dynamic analysis of barge collision for bridge design. Transportation Research Record, 2050(1), 13-25. Fan, W., Liu, Y., Liu, B., and Guo, W. 2016. Dynamic ship-impact load on bridge structures

emphasizing shock spectrum approximation. *Journal of Bridge Engineering*, *21*(10), 04016057.). Lan et al. (Lan, Y., Zhang, R., Jin, L., and Du, X. 2023. Impact performance of BFRP and steel-reinforced concrete beams with different span-to-depth ratios: Numerical and analytical studies. *Science China Technological Sciences*, *66*(2), 301-319.) established a three-dimensional numerical model to study the failure modes of basalt fiber reinforced polymer (BFRP) beams under different span-depth ratios and proposed a simplified model based on energy to predict residual deflection.

Wang et al. (Wang, R., Han, L. H., and Hou, C. C. 2013. Behavior of concrete filled steel tubular (CFST) members under lateral impact: Experiment and FEA model. Journal of Constructional Steel Research, 80, 188-201.) found that the vertical load showed a great effect on the impact resistance of the column. Zhang et al. (Zhang, X., Hao, H., and Li, C. 2016. Experimental investigation of the response of precast segmental columns subjected to impact loading. International Journal of Impact Engineering, 95, 105-124.) applied axial pressure to the RC column in the form of counterweight. Tsang (Tsang, H. H., and Lam, N. T. 2008. Collapse of reinforced concrete column by vehicle impact. Computer-Aided Civil and Infrastructure Engineering, 23(6), 427-436.) showed that high strain rate can improve the stiffness and impact resistance of the column. Some scholars identified the influence of impact mass, impact velocity and reinforcement ratio on the failure mode and dynamic response of RC columns (Wang, W., and Morgenthal, G. 2017. Dynamic analyses of square RC pier column subjected to barge impact using efficient models. Engineering Structures, 151, 20-32.). Sharma (Sharma, H., Gardoni, P., and Hurlebaus, S. 2015. Performance-based probabilistic capacity models and fragility estimates for RC columns subject to vehicle collision. Computer-Aided Civil and Infrastructure Engineering, 30(7), 555-569.) and Sohel et al. (Sohel, K. M. A., Al-Jabri, K., and Al Abri, A. H. S. 2020. Behavior and design of reinforced concrete building columns subjected to low-velocity car impact. Structures, 26, 601-616.) used finite element method to evaluate the vulnerability of RC columns under impact, they observed the dynamic response of steel columns under impact load, and evaluate the influence of impact load on the axial load of RC columns.

The effects of impact velocity, impact mass, slab thickness and reinforcement ratio have been proved to be significant on the failure mode and dynamic response of RC slabs (Othman, H., and Marzouk, H. 2016. An experimental investigation on the effect of steel reinforcement on impact response of reinforced concrete plates. *International Journal of Impact Engineering*, 88, 12-21. Zineddin, M., and Krauthammer, T. 2007. Dynamic response and behavior of reinforced concrete slabs under impact loading. *International Journal of Impact Engineering*, 34(9), 1517-1534. Said, A. M. I., and Mouwainea, E. M. 2022. Experimental investigation on reinforced concrete slabs under high-mass low velocity repeated impact loads. *Structures*, 35, 314-324. Goswami,

A., Adhikary, S. D., and Li, B. 2019. Predicting the punching shear failure of concrete slabs under low velocity impact loading. Engineering Structures, 184, 37-51.; Kumar, V., Igbal, M. A., and Mittal, A. K. 2018. Experimental investigation of prestressed and reinforced concrete plates under falling weight impactor. Thin-Walled Structures, 126, 106-116.). Zineddin (Zineddin, M. 2008. Simulation of reinforced concrete slab behavior under impact loading. AEI 2008: Building Integration Solutions, 1-9.) found that the reinforcement ratio and reinforcement form of the plate can significantly affect the impact resistance of the RC plate. Tai et al. (Tai, Y. S., Chu, T. L., Hu, H. T., and Wu, J. Y. 2011. Dynamic response of a reinforced concrete slab subjected to air blast load. Theoretical and applied fracture mechanics, 56(3), 140-147.) found that the failure of the plate is concentrated at the support with a low reinforcement ratio. Kandil et al. (Kandil, K. S., Nemir, M. T., Ellobody, E. A., and Shahin, R. I. 2014. Strain Rate Effect on the Response of Blast Loaded Reinforced Concrete Slabs. World Journal of Engineering and Technology, 2(04), 260.) showed that the strain rate effect of the concrete and steel material model should be considered in the finite element method (FEM) to simulate the dynamic response of the RC slab under explosion load. Fu (Fu, F. 2013. Dynamic response and robustness of tall buildings under blast loading. Journal of Constructional steel research, 80, 299-307.) has conducted a comprehensive simulation of multi-story buildings under blast loads. Gesund and Kaushik (Gesund, H., and Kaushik, Y. P. 1970. Yield line analysis of punching failures in slabs. International Association for Bridges and Structural Engineering, 30(1), 41-60.) show that the punching shear capacity of RC slabs is highly related to the flexural capacity. Bhatti (Bhatti, A. Q., Kishi, N., and Tan, K. H. 2011. Impact resistant behaviour of RC slab strengthened with FRP sheet. Materials and structures, 44, 1855-1864.) and Soltani (Soltani, H., Khaloo, A., and Sadraie, H. 2020. Dynamic performance enhancement of RC slabs by steel fibers vs. externally bonded GFRP sheets under impact loading. Engineering Structures, 213, 110539.) believe that the fiber reinforced polymer (FRP) can remarkly enhance the impact resistance of the slab.

91

92

93

94

95

96

97

98

99

100

101

102

103

104

105

106

107

108

109

110

111

112

113

114

115

116

117

118

119

120

121

Lefas et al. (Lefas, I. D., Kotsovos, M. D., and Ambraseys, N. N. 1990. Behavior of reinforced concrete structural walls: strength, deformation characteristics, and failure mechanism. *Structural Journal*, *87*(1), 23-31.) studied the influence of different variables on the resistance performance of RC shear walls. Gholipour et al. (Gholipour, M., and Alinia, M. M. 2016. Behavior of multi-story code-designed steel plate shear wall structures regarding bay width. *Journal of Constructional Steel Research*, *122*, 40-56.) believed that a suitable aspect ratio can improve the mechanical performance of the entire structure. Massone et al. (Massone, L. M., Sayre, B. L., and Wallace, J. W. 2017. Load–Deformation responses of slender structural steel reinforced concrete walls. *Engineering Structures*, *140*, 77-88.) used steel sections to replace the longitudinal reinforcement at the side column of RC shear wall and found that there was a certain slip between

steel sections and concrete. Astaneh-Asl (Astaneh-Asl, A. 2002. Seismic behavior and design of composite steel plate shear walls. Moraga, CA, USA: Structural Steel Educational Council.) and Zhao (Zhao, Q., and Astaneh-Asl, A. 2004. Cyclic behavior of traditional and innovative composite shear walls. Journal of Structural Engineering, 130(2), 271-284.) investigated the seismic performance of traditional and innovative composite shear walls under cyclic loading, but did not explore the effects of thinner or thicker concrete walls, as well as different reinforcement ratios or configurations on preventing concrete crushing, controlling cracks, influencing composite action efficiency, and overall performance. Zhou et al. (Zhou, Y., Zhang, X., Yi, F., Sun, J. M., Ni, J., Li, T., and Yi, W. J. 2024. Impact resistance and performance of precast shear walls with various connections under axial and lateral loads. Engineering Structures, 318, 118748.) explored the impact resistance of precast concrete shear walls with various connection types under combined axial compression and lateral impact loads, and proposed a rapid evaluation method for the impact resistance of shear walls. However, the tests were conducted under constant axial compression ratios, impact energies, and specimen geometries, without considering the effects of high axial compression ratios, different impact energies, and various specimen sizes on the impact resistance of PC shear walls. Some scholars have proposed using displacement analysis models to predict the deflection of walls and the strain of materials (Yong, A. C. Y., Lam, N. T. K., Menegon, S. J., and Gad, E. F. 2020a. Cantilevered RC wall subjected to combined static and impact actions. International Journal of Impact Engineering, 143, 103596. Yong, A. C. Y., Lam, N. T. K., Menegon, S. J., and Gad, E. F. 2020b. Experimental and analytical assessment of flexural behavior of cantilevered RC walls subjected to impact actions. Journal of Structural Engineering, 146(4), 04020034.) but the model is applicable to fully cracked RC walls that remain elastic.

122

123

124

125

126

127

128

129

130

131

132

133

134

135

136

137

138

139

140

141

142

143

144

145

146

147

148

149

150

151

152

Although multiple studies on RC shear walls under impact have been mentioned in previous paragraphs, these studies still have limitations. Therefore, a pendulum impact rig was designed and six specimens with different reinforcement ratios, impact energies, and impact positions were tested to investigate the impact resistance of RC shear walls and further explore the resistance mechanism, failure modes, dynamic response, and influencing principles of RC shear walls under impact loads. Moreover the test specimens are designed to simulate the independent inter-floor segments of shear walls in tall buildings (such as the wall between two floors). Different wall heights are set to mainly investigate the influence of aspect ratios on impact responses. The test specimens reflect the bending and punching shear failure modes under local impact, as well as the effect of aspect ratios. Based on the experimental results, the analytical model applicable to the elastoplastic stage was established to

predict the maximum displacement of the components under impact loads. the numerical analysis was conducted by LS-DYNA to realize extended parametric studies (considering different axial compression ratios, wall widths, and impact energies) to better understand the mechanism.

Impact tests

Test Specimens

According to the specification (ACI (American Concrete Institute). 2014. Building code requirements for structural concrete (ACI 318-14) and commentary (318R-14). ACI 318. Farmington Hills, MI: ACI.), the 1/2 scaled specimens were fabricated with the wall height of 1800 or 1200 mm, the width of 1200 mm, and a thickness of 150 mm. During concrete casting, three standard cylindrical concrete specimens were prepared and cured under standard conditions for 28 days. The measured compressive strength was 36 MPa, and the elastic modulus was 34.1 GPa. The detailed configuration of the specimens is summarized in **Table 1**.

Table 1. Specimen design parameters

Test ID	Wall height	Reinforcement ratio	Impact	Drop height (m)	
	(m)	(%)	location		
H1.8-1/2-1.5	1.8	0.52%	1/2	1.5	
H1.8-1/3-1.5	1.8	0.52%	1/3	1.5	
L1.8-1/2-1.5	1.8	0.33%	1/2	1.5	
L1.8-1/2-2.0	1.8	0.33%	1/2	2.0	
H1.2-1/2-1.5	1.2	0.52%	1/2	1.5	
H1.2-1/2-2.0	1.2	0.52%	1/2	2.0	

Note: H and L represent walls with higher and lower reinforcement ratios, respectively; 1.8 and 1.2 represent the height of the wall respectively; 1/2 and 1/3 represent the position of impact point respectively.

As shown in Fig. 1, the hot-rolled ribbed, grade 400 (HRB400) steel bars (diameter 10 or 8 mm) were used as the vertical and horizontal distributed reinforcement and stirrups of the specimens. HPB400 steel bars (diameter 6 mm) were adopted as tie bars. The vertical reinforcement of specimens LN1.8-1/2-1.5 and LN1.8-1/2-2.0 was C8@200, while that of the remaining specimens was C10@200. All specimens had horizontal distributed reinforcement of C8@200 and stirrups of C8@150. The concrete cover thickness was uniformly 20 mm. Table 2 presents the mechanical properties of the steel bars.

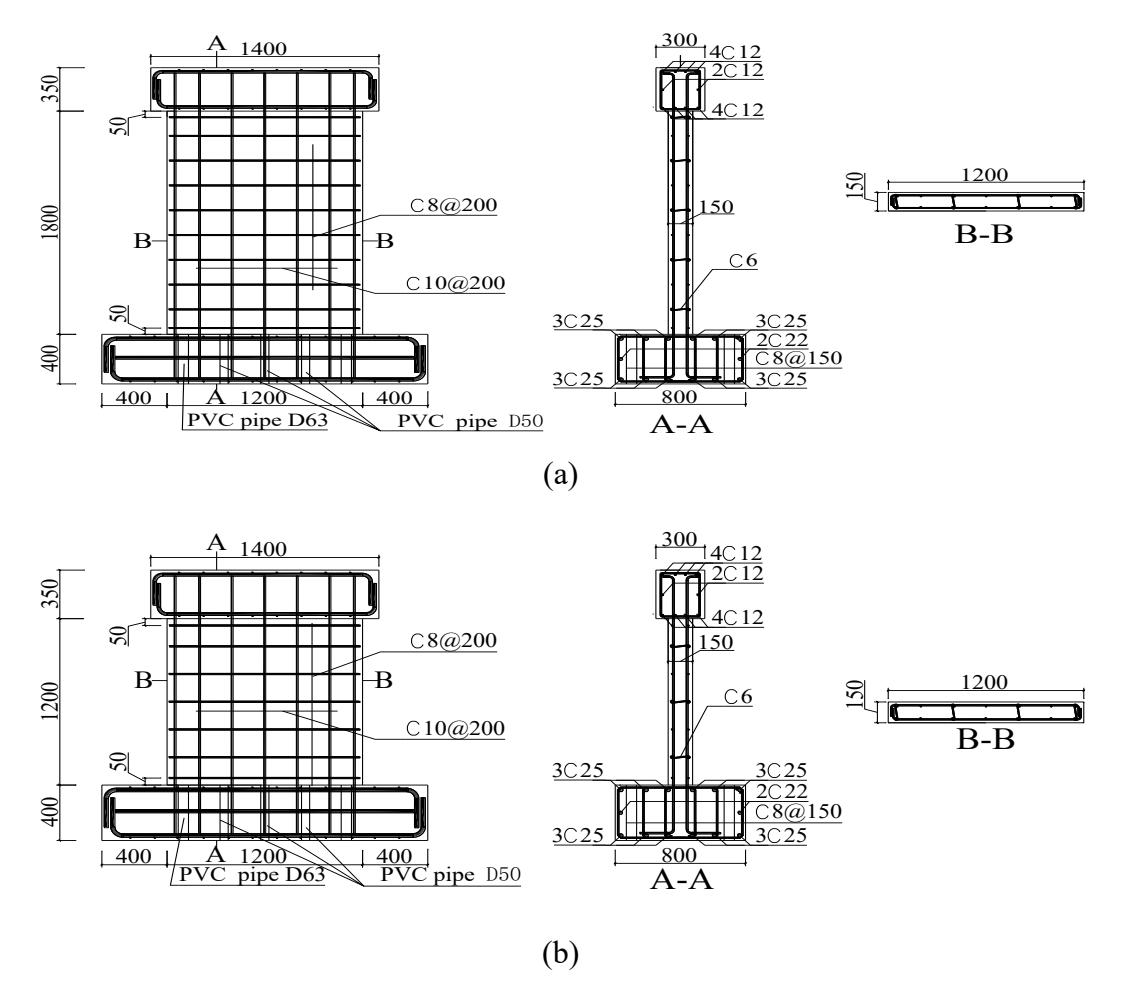


Fig. 1. Reinforcement diagram: (a) H1.8-1/2-1.5; and (b) H1.2-1/2-1.5.

Table 2. Material properties of steel bars

			1 1		
Type of steel bars	Diameter (mm)	Elastic	Yield	Ultimate	Ultimate elongation
		modulus	strength	strength	percentage
		(GPa)	(MPa)	(MPa)	(%)
HRB400 steel bars	8	205	467	665	11.6
	10	207	483	628	11.0
HPB400 steel bars	6	208	466	661	11.7

Experimental setup

The test utilized a specialized pendulum impact rig, as shown in Fig. 2. The pendulum had a maximum impact radius of 5.3 m and a maximum impact mass of 2000 kg. A 150-kN axial load was pre-applied to all specimens via a hydraulic jack on the loading beam. The foundation beam was anchored to the steel bearing through six M36 bolts in pre-embedded PVC sleeves. Horizontal restraint was provided by an A-frame steel girder, and a self-equilibrating system was established using four M48 long bolts connecting the hydraulic jack, top support, and foundation beam. Similar instrumentation can be seen in Huo (Qu, H., Huo, J., Xu, C., and Fu, F. 2014. Numerical studies on dynamic

behavior of tubular T-joint subjected to impact loading. International Journal of Impact Engineering, 67, 12-26.).

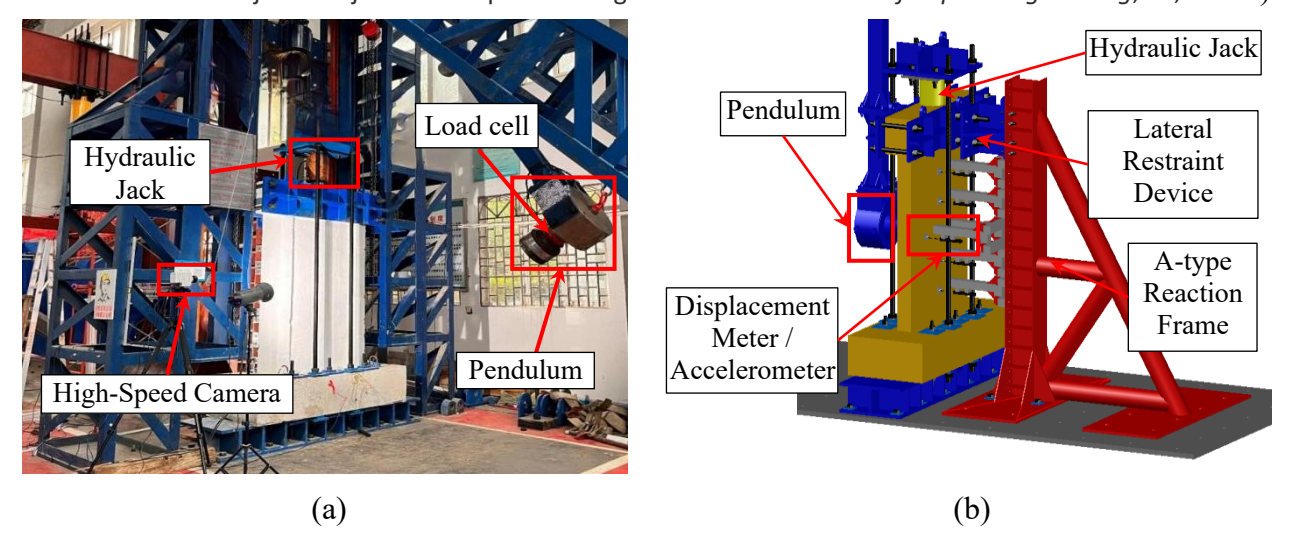


Fig. 2. Test setup and instrumentation layout of tests: (a) photo; and (b) schematic view.

Test Plan

In this test, data were collected by a dynamic signal acquisition system and high-speed camera with 50 kHz and 5000 fps, respectively. A load cell mounted on the pendulum required data calibration with a 1.10 correction factor due to its indirect loading configuration. The displacement and acceleration transducers were attached on the wall at 300 mm intervals, as shown in **Fig. 3**, where "D" and "A" label displacement and acceleration transducers, respectively.

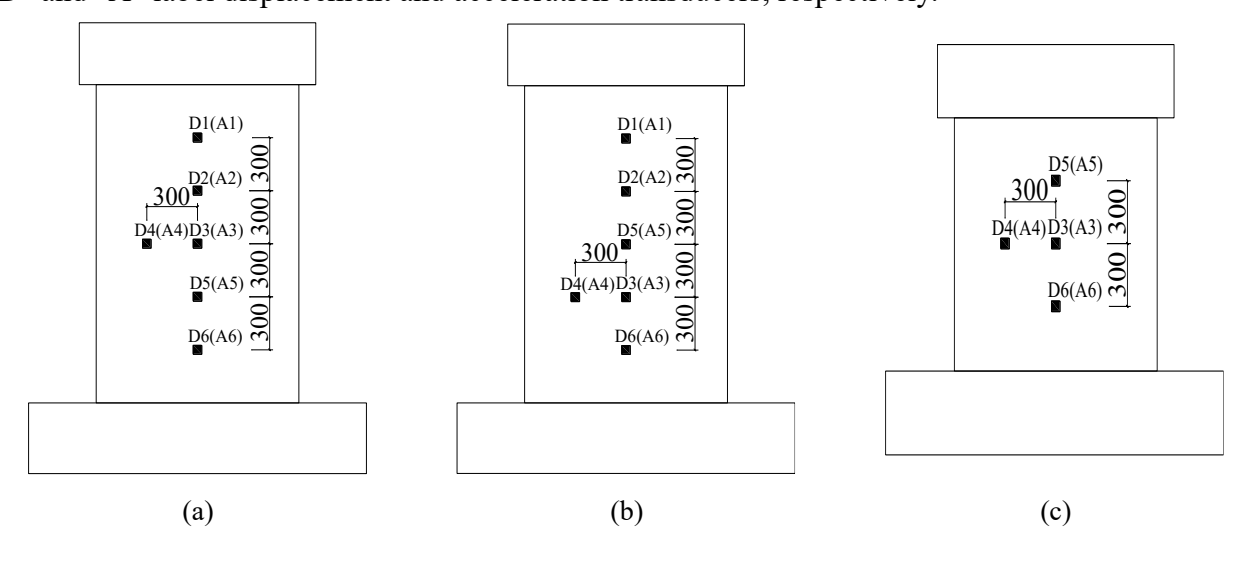


Fig. 3. Diagram of measuring point layout: (a)1.8-1/2 series; (b)1.8-1/3 series; and (c)1.2-1/2 series

Experimental Results

Impact Load

Fig. 4 compares impact force time-history curves of all specimens. Though all curves in shear wall specimens even with different variables exhibit similar trends, peak impact forces and overall

response times differ significantly. Specifically, the increment of drop height and reinforcement ratio raises peak impact force due to their influence on contact stiffness and impact energy. For instance, in **Fig. 4**(c), peak force increases from 1423.4 kN to 1685.8 kN (18.4% increase). Conversely, variations in wall height and impact position reduce overall response time: **Fig. 4**(a) and **Fig. 4**(e) show reductions of 22.7% and 17.4%, respectively, alongside increased impact force plateau values.

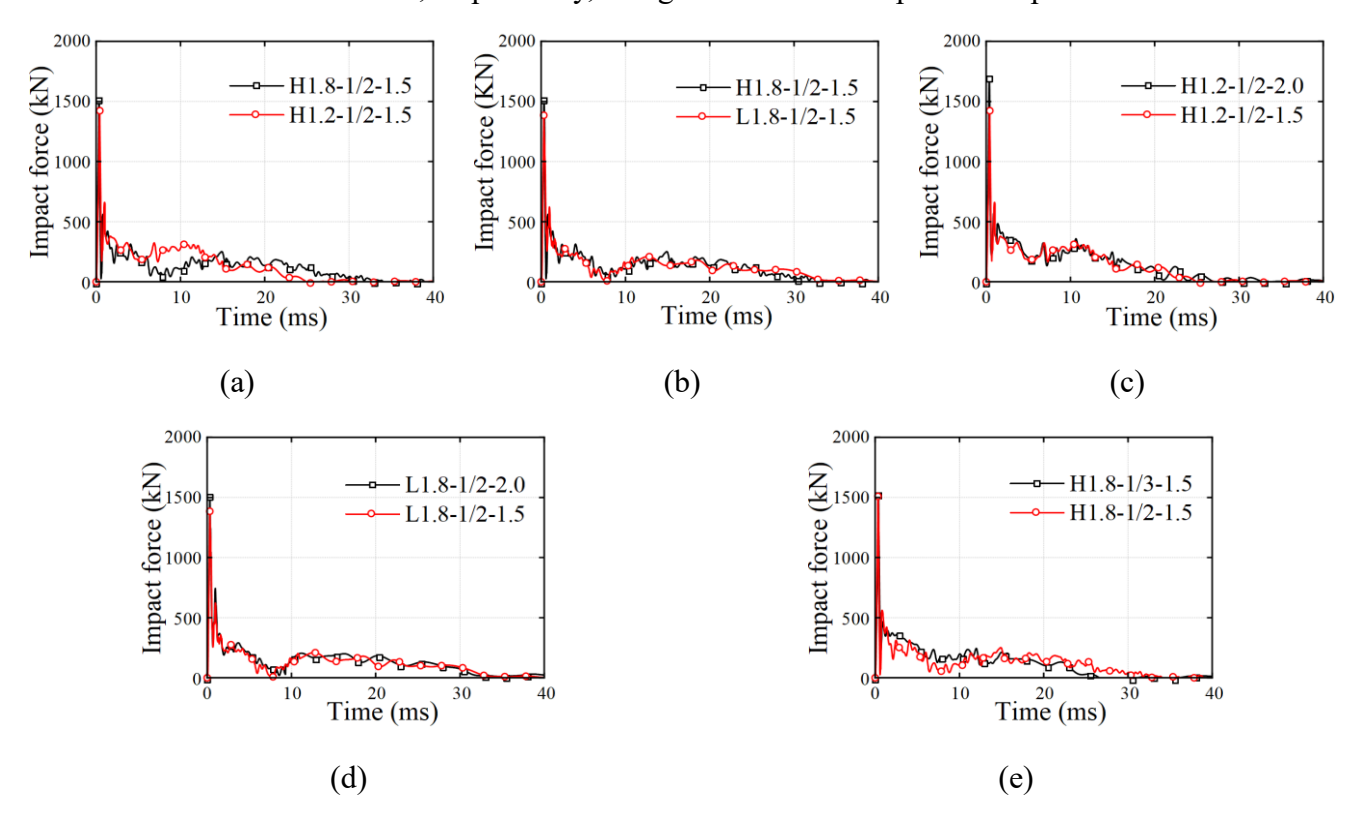


Fig. 4. Comparison of time history curves of impact force under different variables: (a) wall height; (b) reinforcement ratio; (c) drop height; (d) drop height; and (e) impact position.

Crack patterns

Fig. 5Fig. 9 illustrate crack progress in the typical specimen. Due to the limitation of the test site, only the right half of the specimen is shown. Specimen H1.8-1/2-1.5 exhibited a circumferential crack (radius of about 150 mm) at 0.6 ms, followed by radial expansion at 3 ms and dominant global response at 7 ms. Horizontal cracks at the impact site increased in number and width thereafter, with crack development completed at 20 ms. Meanwhile, specimen H1.8-1/3-1.5 developed horizontal cracks at the impact point at 8 ms. By 13 ms, owing to the impact position being separated from the upper loading beam, the global response involved resisting higher bending moments, which induced horizontal transverse cracks of 400 mm above the impact site. On the contrary, the reduction of the reinforcement ratio will accelerate the crack progression, see in Fig. 7 and Fig. 8: horizontal transverse cracks initiated at 3 ms, expanded significantly by 7 ms, and stabilized by 20 ms.

Failure modes

216

217

218

219

220

221

222

223

224

225

226

227

228

229

230

231

232

233

234

235

236

Fig. 10Fig. 15 illustrate the failure modes of the specimen's front, back, and side faces.

Front face failure mode: specimen H1.8-1/2-1.5 exhibited distinct horizontal cracks in its upper and lower regions, whereas specimen H1.2-1/2-1.5 showed no obvious cracking, as illustrated in Fig. 10 and Fig. 14. This distinction can be attributed to the higher global stiffness of the shorter specimen, which enhanced impact resistance. As shown in Fig. 12(c), for specimen L1.8-1/2-1.5, lower reinforcement content reduced flexural capacity, inducing a midspan horizontal bending crack that traversed the whole cross-section, leading to global bending of the side face. The increment of impact energy exacerbated cracking in L1.8-1/2-2.0, with concrete crushing followed by spalling-characteristic of flexural failure.

Back face failure mode: the back face exhibited combined flexural and punching shear failure. Whereas the flexural-induced horizontal cracks progressed circumferentially at the impact site. The cracking propagation is radial with concrete spalling—characteristic of punching shear failure. Increasing impact energy amplified crack density at the impact site and expanded spalling areas. As long as the impact point was changed, flexural cracks concentrated above the new impact position, reflecting altered stress distribution, see in Fig. 11(b).

Two failure modes were observed from the experimental results: punching shear failure (annular cracking at the impact site with radial propagation) and flexural failure (mid-span area horizontal bending cracks).



(a) 0.6 ms



(b) 3 ms

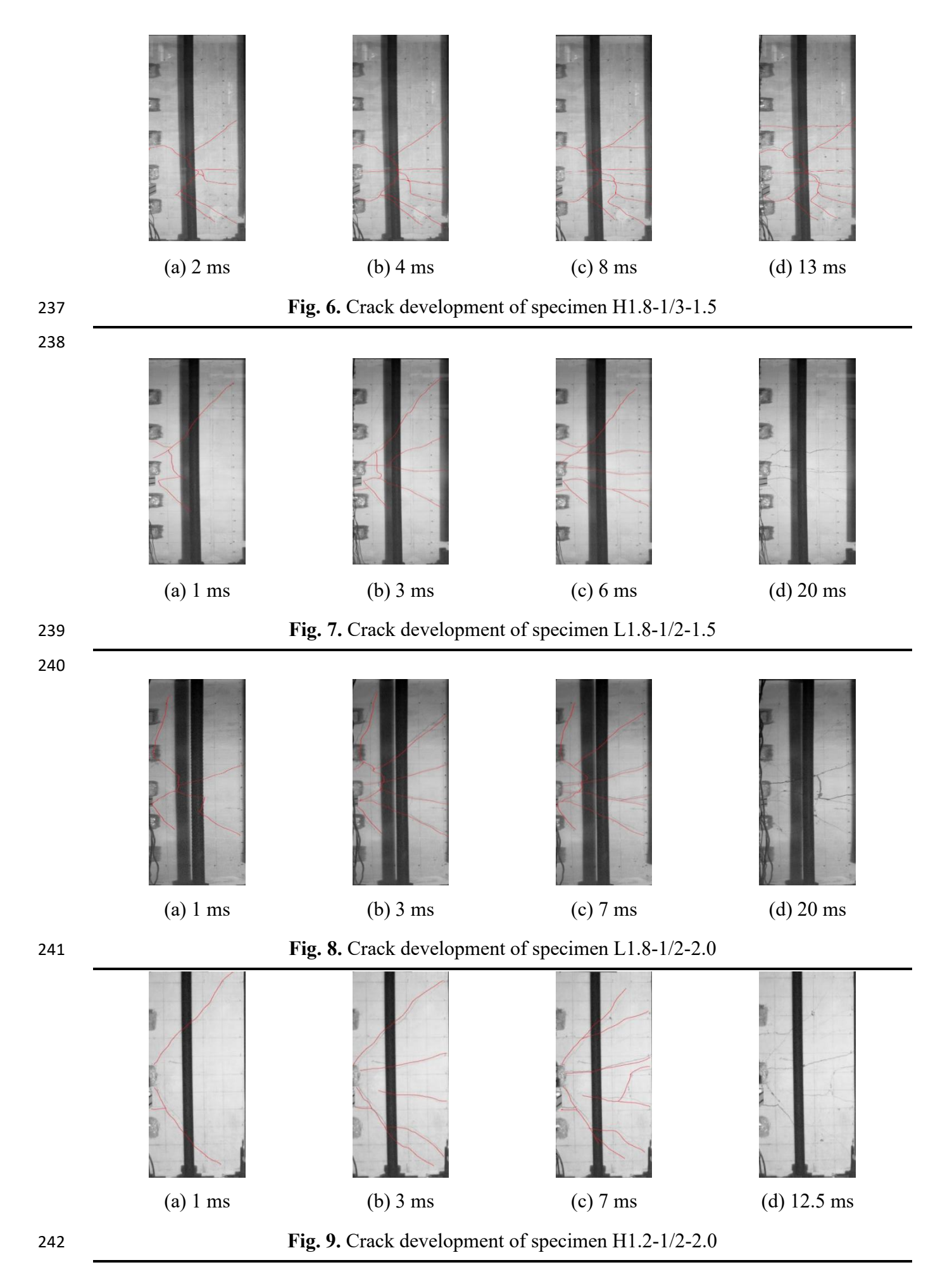


(c) 7 ms



(d) 20 ms

Fig. 5. Crack development of specimen H1.8-1/2-1.5



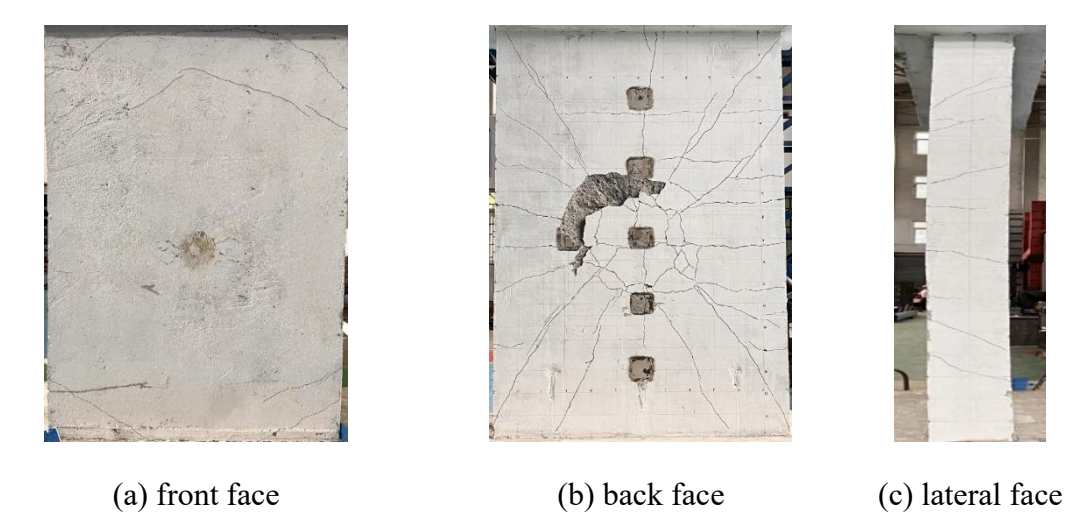


Fig. 10. The failure mode of the specimen H1.8-1/2-1.5

(a) front face (b) back face (c) lateral face

Fig. 11. The failure mode of the specimen H1.8-1/3-1.5

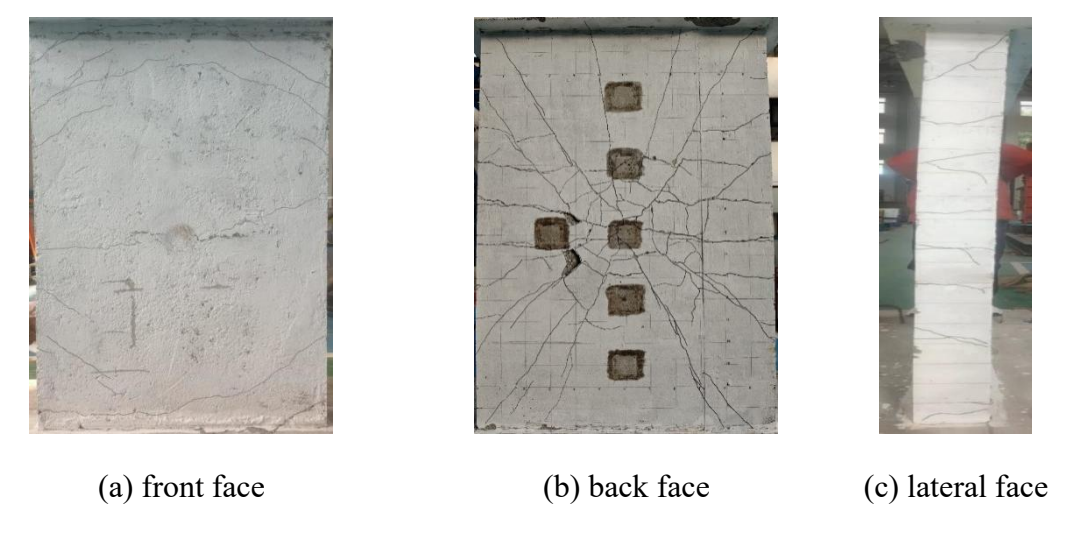


Fig. 12. The failure mode of the specimen L1.8-1/2-1.5

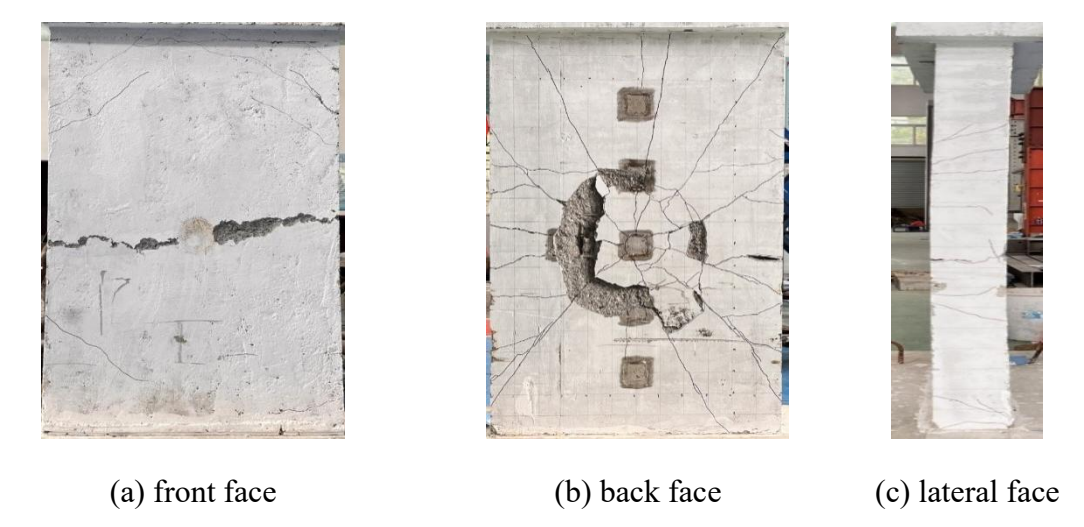


Fig. 13. The failure mode of the specimen L1.8-1/2-2.0

(a) front face



(b) back face



(c) lateral face

Fig. 14. The failure mode of the specimen H1.2-1/2-1.5

252253

254

255

250

251



(a) front face



(b) back face



(c) lateral face

Fig. 15. The failure mode of the specimen H1.2-1/2-2.0

Displacement

For the measurement of specimen displacement, as the foundation beam at the specimen base is fixed by bolts with limited horizontal restraint, the foundation beam may undergo horizontal displacement under impact loading. To this end, rod-type linear displacement sensors are used to monitor the horizontal and vertical displacements of the foundation beam as shown in **Fig. 16**, and the displacement time-history curves of all measuring points on the specimen are corrected based on those of the foundation beam. **Fig. 17** shows the foundation beam displacement time-history curves for some specimens. Results show that the vertical displacement of the foundation beam is relatively small, with horizontal displacement controlled within 8 mm.

Fig. 18 shows the displacement-time history curves for all measuring points on the specimens. Large-scale concrete spalling during testing caused partial measuring points to detach from the specimens, leading to inaccurate data, such as D5 of H1.8-1/2-1.5, D5 of H1.2-1/2-1.5, and D6 of H1.2-1/2-2.0. In H1.8-1/2-1.5, L1.8-1/2-1.5, and L1.8-1/2-2.0, the peak displacement values at D1 and D6, as well as D2 and D5 (excluding the damaged D5 in H1.8-1/2-1.5), are relatively close. The peak displacement at D3 is higher than that at D2, which in turn exceeds that at D1. This indicates that deformations at D1 and D6 primarily result from the flexural resistance of the wall, while a combination of overall bending and local shear causes those at D2 and D5.

Compared with H1.8-1/2-1.5, the impact point position (Fig. 3) of specimen H1.8-1/3-1.5 in Fig. 18. Displacement time history curves of all measuring points of the specimen: (a) H1.8-1/2-1.5; (b) H1.8-1/3-1.5; (c) L1.8-1/2-1.5; (d) L1.8-1/2-2.0; (e) H1.2-1/2-1.5; and (f) H1.2-1/2-2.0. is closer to the bottom foundation beam, leading to more restrictive boundary constraints at D6 and resulting in lower peak displacement at D6 compared to D5 and D2. Fig. 18. Displacement time history curves of all measuring points of the specimen: (a) H1.8-1/2-1.5; (b) H1.8-1/3-1.5; (c) L1.8-1/2-1.5; (d) L1.8-1/2-2.0; (e) H1.2-1/2-1.5; and (f) H1.2-1/2-2.0. show that the deformation recovery coefficients of both specimens exceed 0.4, indicating a significant weakening in the deformation recovery capacity due to their lower wall height, higher overall flexural stiffness, and proneness to shear failure.

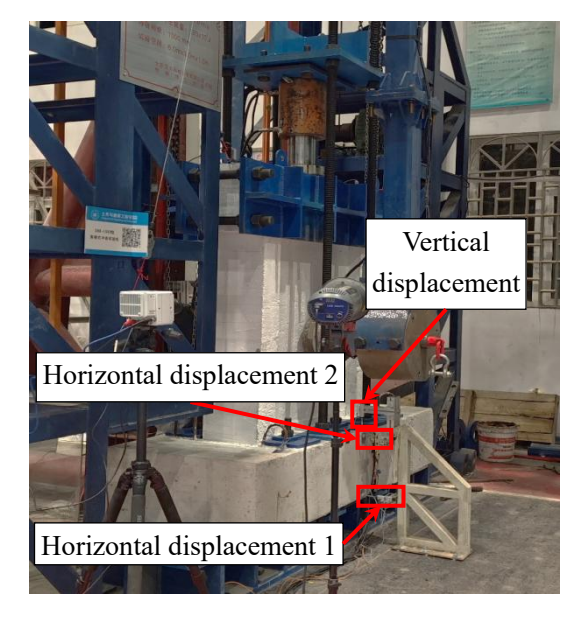
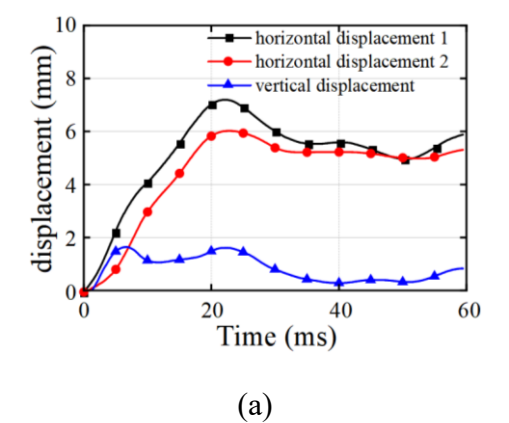


Fig. 16. Diagram of displacement measurement device for bottom foundation beam



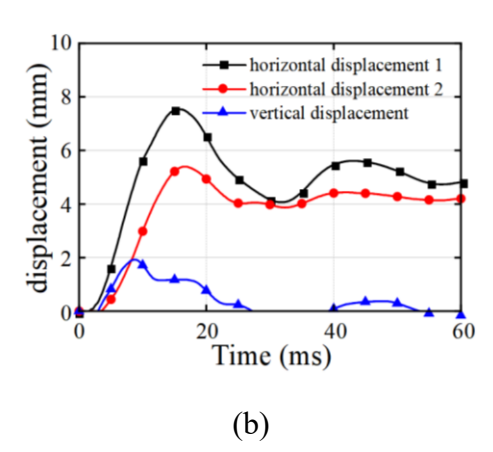
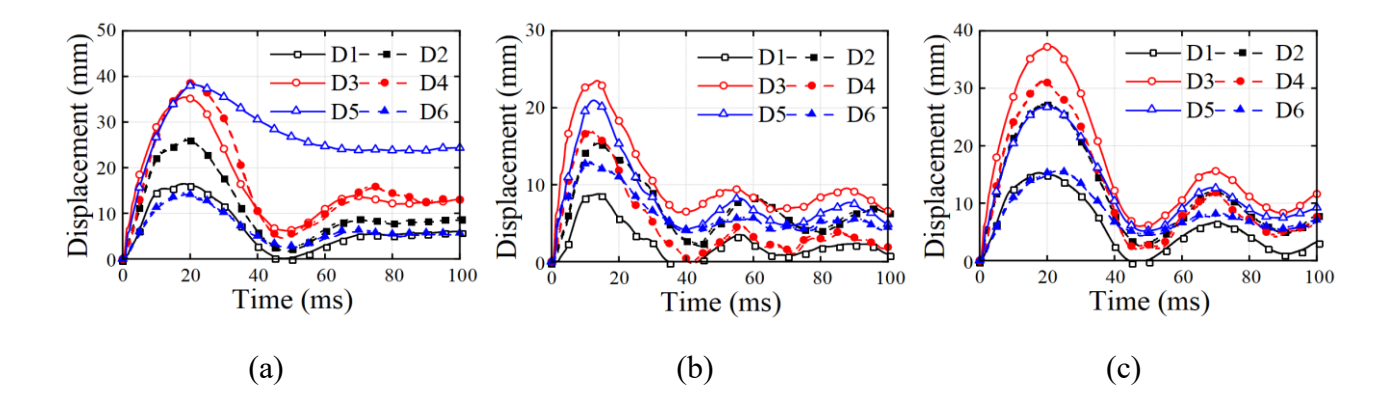


Fig. 17. Displacement time history curve of specimen foundation beam: (a) L1.8-1/2-1.5; and (b) H1.2-1/2-1.5



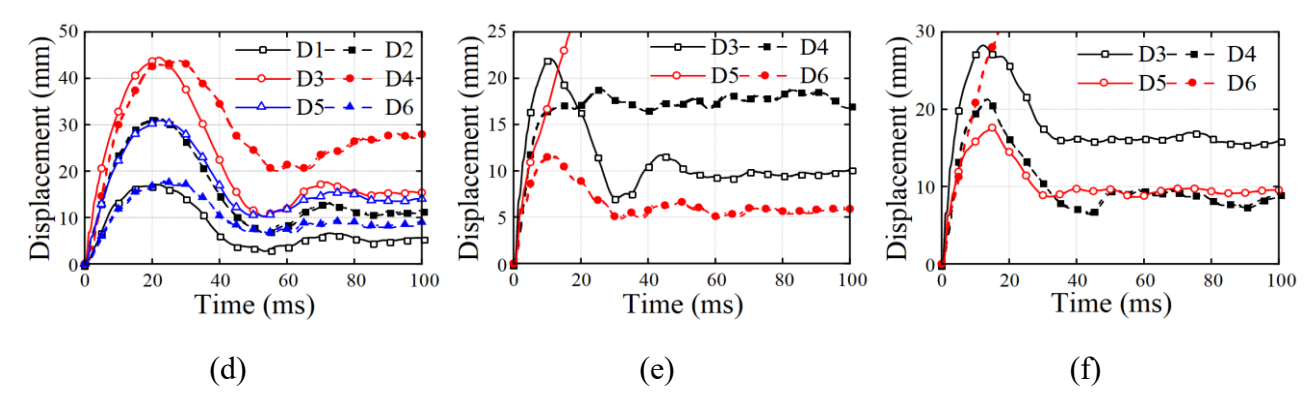


Fig. 18. Displacement time history curves of all measuring points of the specimen: (a) H1.8-1/2-1.5; (b) H1.8-1/3-1.5; (c) L1.8-1/2-1.5; (d) L1.8-1/2-2.0; (e) H1.2-1/2-1.5; and (f) H1.2-1/2-2.0.

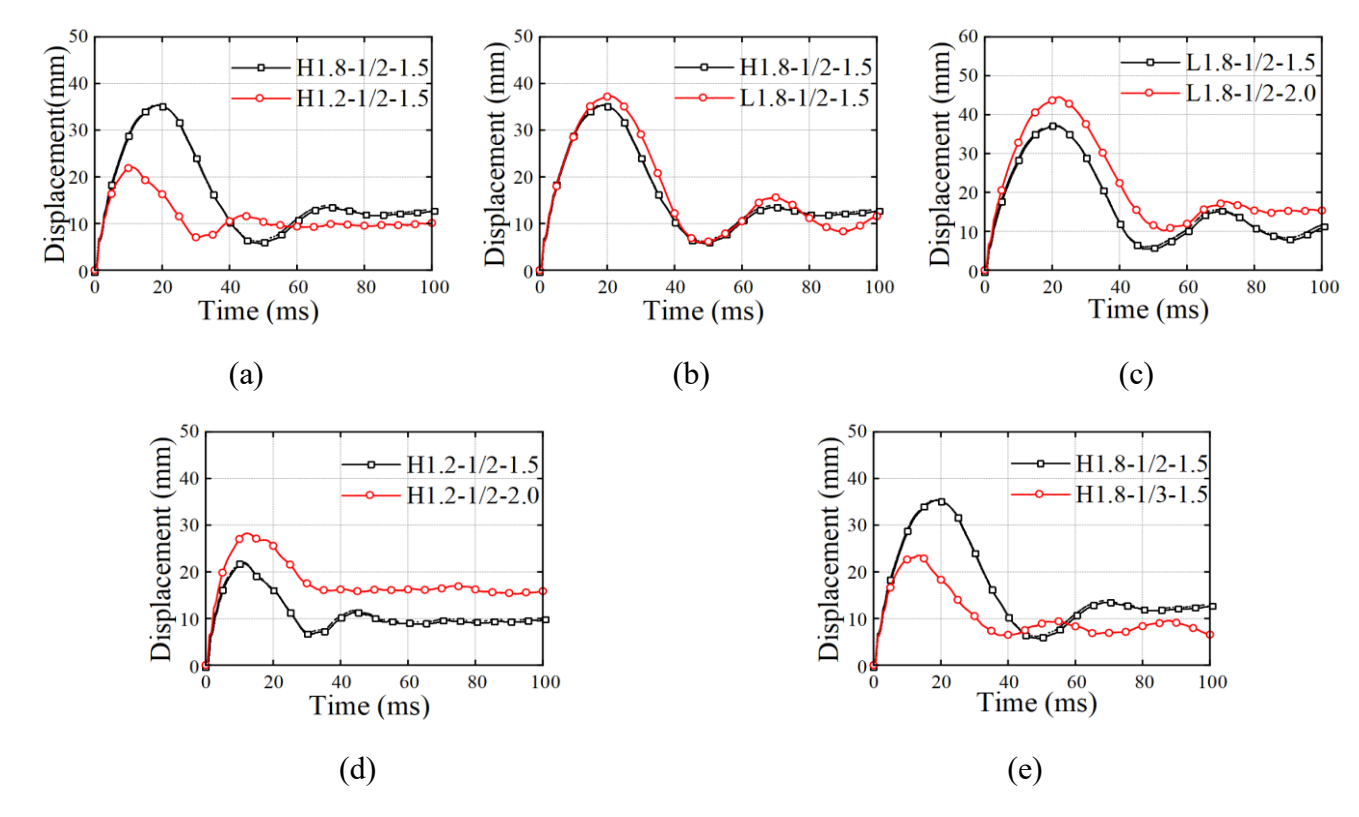


Fig. 19. Time history curves of D3 measuring points displacement under different variables: (a) wall height; (b) reinforcement ratio; (c) drop height; (d) drop height; and (e) impact position.

Table 3. Characteristic values of displacement time history curves

Test ID	D_m (mm)	T_d (ms)	D_r (mm)	Deformation recovery coefficient
HN1.8-1/2-1.5	35.2	18.9	12.1	0.34
HN1.8-1/3-1.5	23.5	14.1	7.5	0.32
LN1.8-1/2-1.5	37.2	18.8	9.6	0.26
LN1.8-1/2-2.0	44.4	22.1	15.	0.34
HN1.2-1/2-1.5	22.0	11.1	9.4	0.43
HN1.2-1/2-2.0	28.2	12.5	16.1	0.57

- Note: D_m represents the peak displacement; T_d represents the time required to reach the peak displacement; D_r
- represents the residual displacement.
- To analyze specimen displacements under different variables, D3 points (impact point) were
- selected. Fig. 19 compares displacement-time history curves for D3 across specimens, with
- 296 characteristic features listed in
- **Table 3**.

Reducing wall height from 1.8 m to 1.2 m in H1.2-1/2-1.5 increased global stiffness, decreasing peak displacement by 37.5% and peak displacement time by 41.3% compared to H1.8-1/2-1.5. Lowering reinforcement ratio in L1.8-1/2-1.5 reduced global stiffness, causing a 5.7% increase in peak displacement relative to H1.8-1/2-1.5, while peak displacement times remained comparable between the two specimens. As shown in **Fig. 19.** Time history curves of D3 measuring points displacement under different variables: (a) wall height; (b) reinforcement ratio; (c) drop height; (d) drop height; and (e) impact position., increasing impact energy in L1.8-1/2-2.0 and H1.2-1/2-2.0 induced 19.4% and 28.2% increases in peak displacement and 17.6% and 12.6% increases in peak displacement time, respectively. Elevated drop heights consistently increased both response parameters, with more prominent effects at larger height increments. In **Fig. 19.** Time history curves of D3 measuring points displacement under different variables: (a) wall height; (b) reinforcement ratio; (c) drop height; (d) drop height; and (e) impact position., H1.8-1/3-1.5's impact position closer to the bottom foundation beam enhanced boundary constraints, reducing peak displacement and peak time by 33.2% and 25.4% compared to H1.8-1/2-1.5 under impact loading.

Deflected shapes

Based on the time-displacement histories of each measuring point as shown in Fig. 18, the deflected shapes of each specimen were plotted. Data from some measuring points were excluded due to their detachment during the test, as previously described.

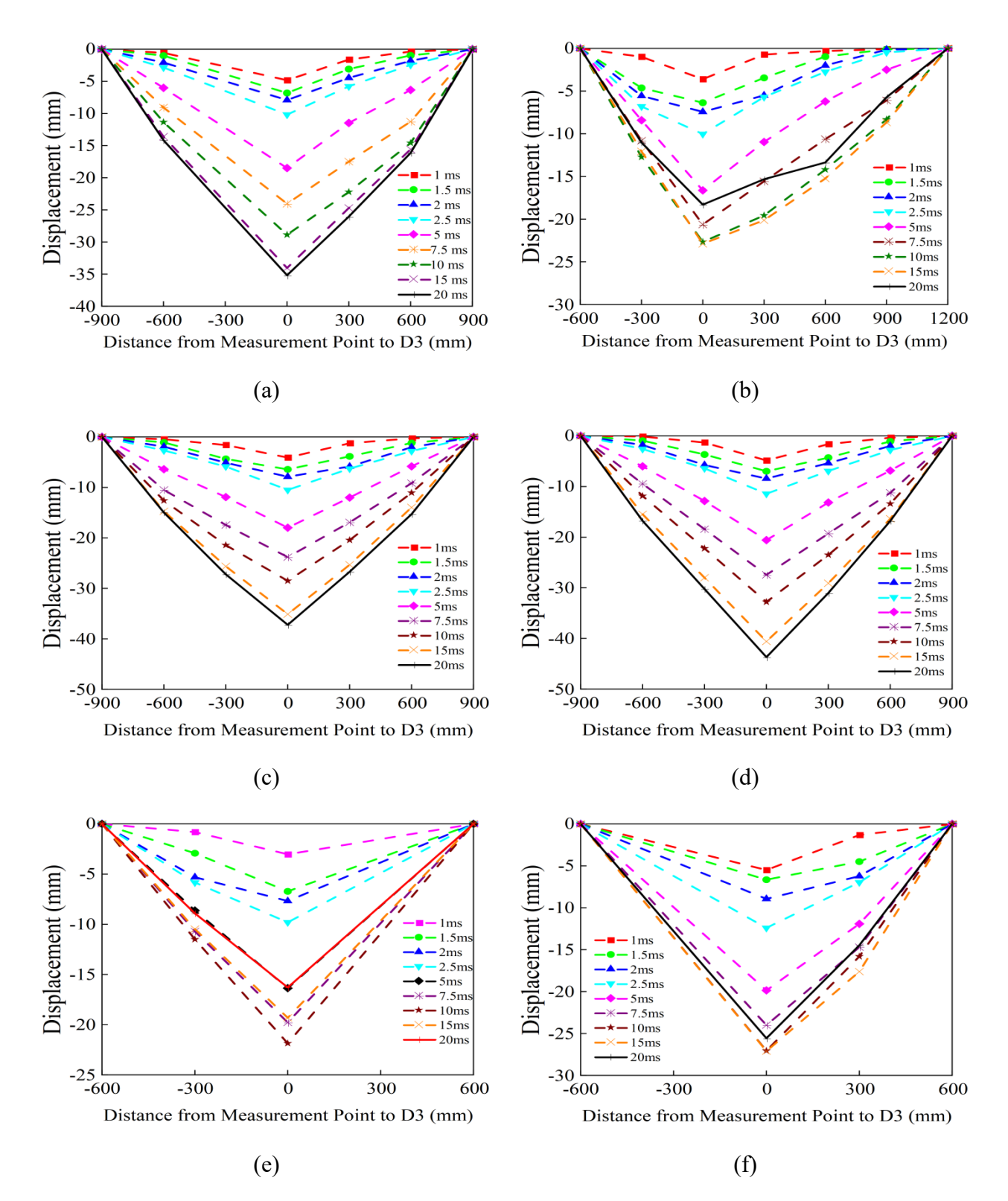


Fig. 20. Comparison of deflected shapes of specimens: (a) H1.8-1/2-1.5; (b) H1.8-1/3-1.5; (c) L1.8-1/2-1.5; (d) L1.8-1/2-2.0; (e) H1.2-1/2-1.5; and (f) H1.2-1/2-2.0.

As illustrated in **Fig. 20**, an overall flexural response was obvious in the early loading stage. Notably, the deflection in the impacted area increased much more rapidly than that in the unloaded area, indicating the punching shear behavior, which was accompanied by the propagation of shear cracks and the formation of a punching cone.

Energy Consumption

The Law of Conservation of Energy was applied to analyze the data from the impact testing. Fig. 21 shows the impact force-displacement curves of specimens. Due to multiple impacts and rebounds of the pendulum, the VIC-2D material dynamic characterization measurement system was used to monitor the velocity of the first impact. The kinetic energy loss of the pendulum was calculated based on the difference in velocity before and after the first impact, and the results were shown in Table 4.

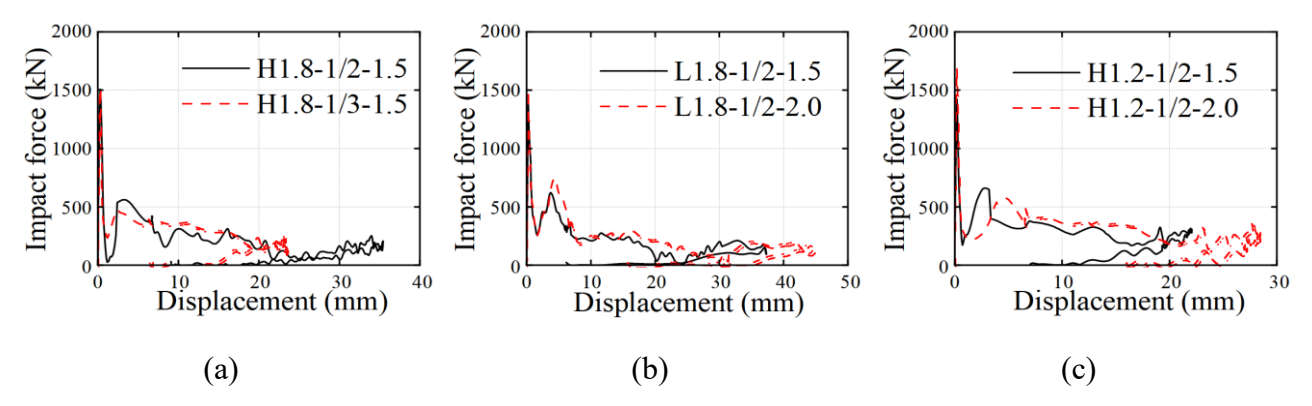


Fig. 21. Force-displacement curves: (a) H1.8-1/2-1.5, H1.8-1/3-1.5; (b) L1.8-1/2-1.5, L1.8-1/2-2.0; and (c) H1.2-1/2-1.5, H1.2-1/2-2.0.

Table 4. Statistics of energy dissipation of each specimen under impact load

Test ID	Energy dissipation (kN·mm)	Impact velocity (mm/ms)	Rebound velocity (mm/ms)	Impact energy (J)	Energy absorption rate (%)
HN1.8-1/2-1.5	6896.4	5.22	1.83	9559.8	72.14%
HN1.8-1/3-1.5	6222.1	5.27	1.15	10580.16	58.81%
LN1.8-1/2-1.5	6945.2	5.22	1.89	9470.52	73.33%
LN1.8-1/2-2.0	9461.0	5.92	1.76	12779.52	74.03%
HN1.2-1/2-1.5	5878.6	5.22	1.29	10233.72	57.44%
HN1.2-1/2-2.0	8653.2	6.01	0.77	14210.88	60.89%

Note: energy absorption rate is calculated as ratio of energy dissipation to impact energy.

With the decrease of the wall height, the specimen's overall stiffness increases, and the deformation energy absorption reduces as well as the energy absorption rate. Reducing reinforcement ratio decreases overall stiffness, enhances deformation capacity, increases deformation energy absorption, and raises energy absorption rate. A closer impact position to the bottom increases bending stiffness below the impact point, reduces deformation energy absorption, and lowers the

energy absorption rate. Increasing the drop height elevates impact energy, increases specimen energy absorption, and increases the energy absorption rate. Notably, at constant impact energy, specimen energy absorption performance correlates primarily with overall stiffness: higher stiffness corresponds to poorer energy absorption.

Numerical Simulation Analysis

338

339

340

341

342

343

344

345

346

347

348

349

350

351

352

353

354

355

356

357

358

359

360

361

362

363

364

365

366

367

Finite Element Model and Material Constitutive

The finite element model of all specimens was built using LS-DYNA (Hallquist, J. O. 2007. *LS-DYNA-Keyword user's manual, version 971, livermore soft*. California, USA: Technology Corporation (LSTC).), as shown in **Fig. 22**.

The bottom nodes of the foundation beam were constrained via the *BOUNDARY_SPC_SET keyword, while double steel plates restrained the horizontal sides of the loading beam. Axial pressure was applied using the *LOAD_RIGID_BODY keyword, with a top steel plate limiting upward vertical displacement of the loading beam.

There is no bond failure between steel bar and concrete in the test, so steel-concrete coupling utilized the *CONSTRAINED LAGRANGE IN SOLID keyword. Concrete-hammer contact employed *CONTACT ERODING SINGLE SURFACE to maintain effectiveness after element failure, and the *INITIAL VELOCITY GENERATION keyword applied initial velocity to the hammer. The constitutive model of concrete is CSCM model (Murray, Y. D. 2007. Users manual for LS-DYNA concrete material model 159. United States: Federal Highway AdministrationWu, Y., Crawford, J. E., and Magallanes, J. M. 2012. Performance of LS-DYNA concrete constitutive models. 12th International LS-DYNA users conference, 1, 1-14.; Pham, A. T., Tan, K. H., and Yu, J. 2017. Numerical investigations on static and dynamic responses of reinforced concrete sub-assemblages under progressive collapse. Engineering Structures, 149, 2-20.), with material failure simulated via a strain-based erosion algorithm to effectively capture crack development. Steel bars utilized the *MAT PLASTIC KINEMATIC bilinear elastoplastic material model, incorporating strain rate effects described by the Cowper-Symonds model (Ross, T. J., and Krawinkler, H. 1985. Impulsive direct shear failure in RC slabs. Journal of Structural Engineering, 111(8), 1661-1677.). The hammer head adopted the *MAT RIGID rigid body model, while steel plates used the *MAT ELASTIC linear elastic model. Single-point integral solid elements (20×20×20 mm) were applied to the hammer and bearing components.

Numerical model validation

Numerical and experimental results are compared in Fig. 23-Fig. 25.

Fig. 23 compares the failure modes of all specimens between numerical simulation and experimental observation. Simulation-predicted failure modes predominantly feature annular cracks at the impact point, propagating to surrounding areas, accompanied by horizontal transverse cracks in the impacted area. Crack development and failure modes show a very good agreement with experimental observations. Fig. 24 presents the comparison of impact force time history curves between tests and numerical simulations for all specimens. Due to the inability of numerical models to accurately simulate the failure state of large-scale concrete spalling, the simulated plateau force values are generally higher than experimental results. Additionally, with less signal interference in numerical analysis, the obtained curves are smoother. But these are within a reasonable range. Fig. 24. Impact force time history curves by test and numerical simulation: (a) H1.8-1/2-1.5; (b) H1.8-1/3-1.5; (c) L1.8-1/2-1.5; (d) L1.8-1/2-2.0; (e) H1.2-1/2-1.5; and (f) H1.2-1/2-2.0. presents convergence studies on specimen H1.8-1/2-1.5 to assess mesh size sensitivity (10 mm, 15 mm, 20 mm) for constituent materials. A 10 mm mesh, balancing accuracy and computational efficiency, was chosen for subsequent FE analysis. Fig. 25 presents the comparison of displacement time history curves at the impact point between tests and numerical simulations. The numerical results agree well with the experimental data, with minor discrepancies within a reasonable range (10%). Overall, the developed numerical model can effectively and precisely simulate the failure modes and dynamic responses of the specimens.

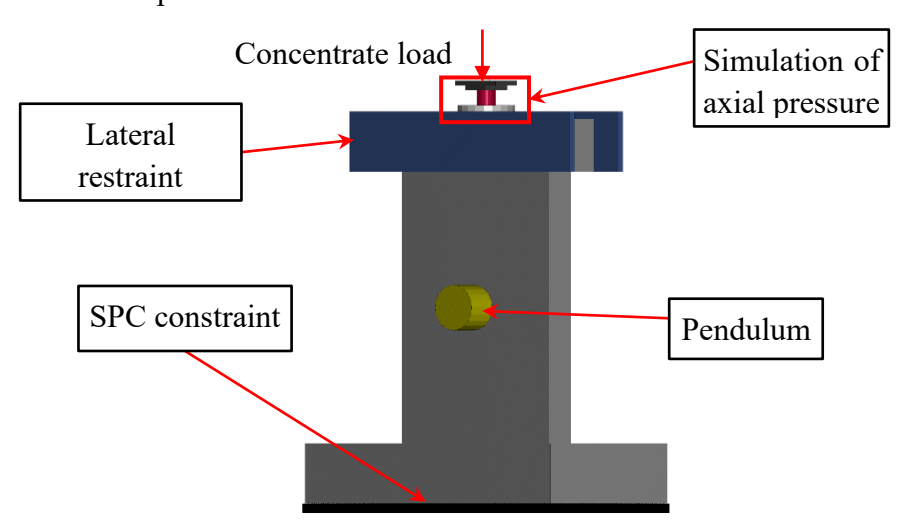


Fig. 22. Specimen finite element analysis model

387

368

369

370

371

372

373

374

375

376

377

378

379

380

381

382

383

384

385

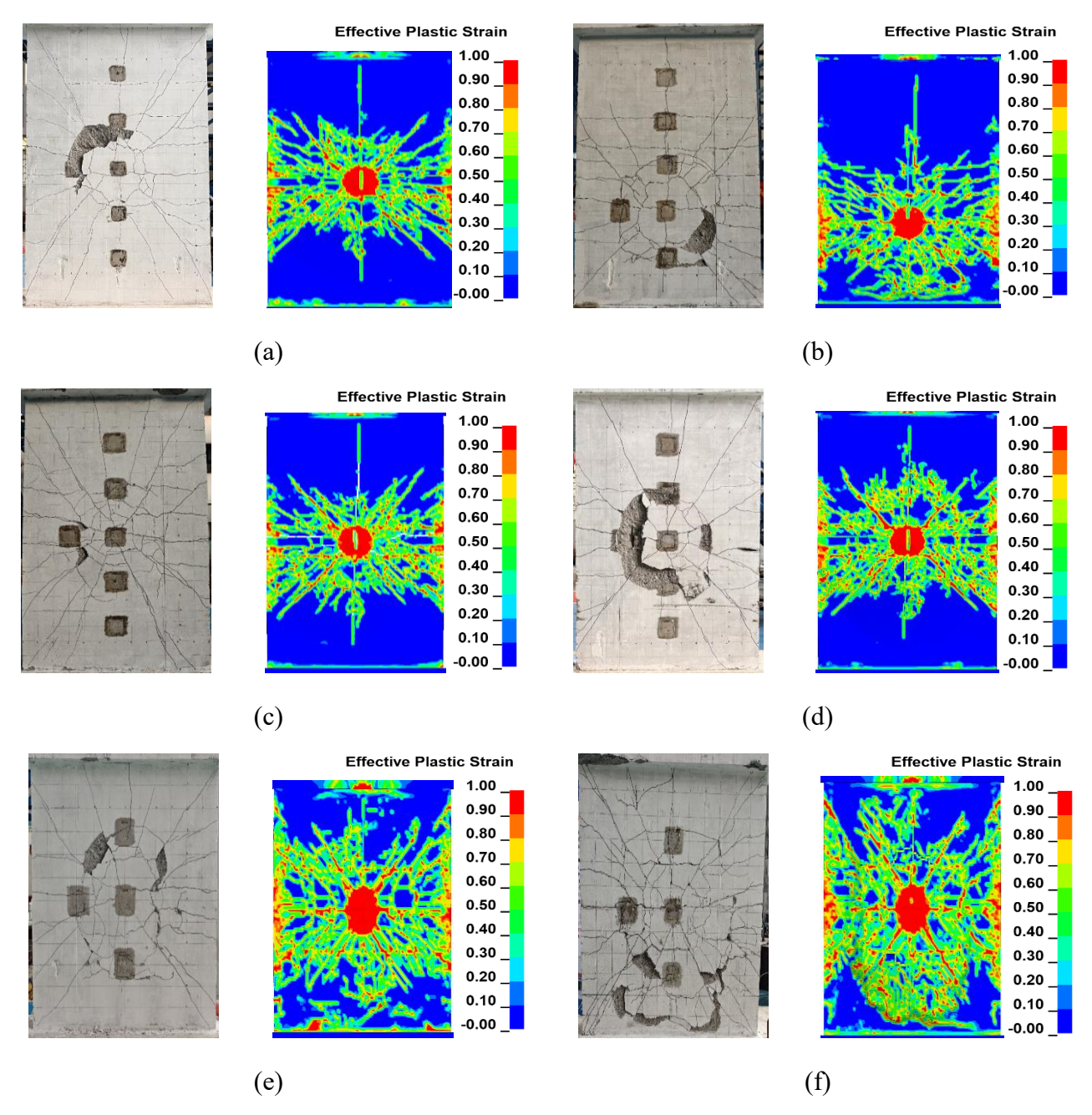
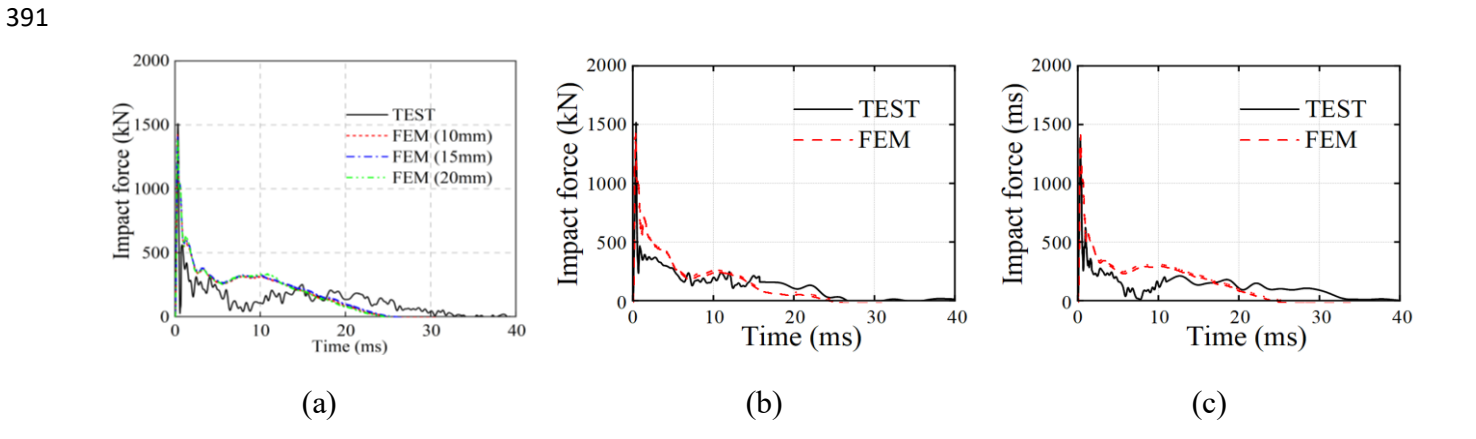


Fig. 23. Comparison of failure modes by test and numerical simulation: (a)H1.8-1/2-1.5; (b) H1.8-1/3-1.5; (c) L1.8-1/2-1.5; (d) L1.8-1/2-2.0; (e) H1.2-1/2-1.5; and (f) H1.2-1/2-2.0.



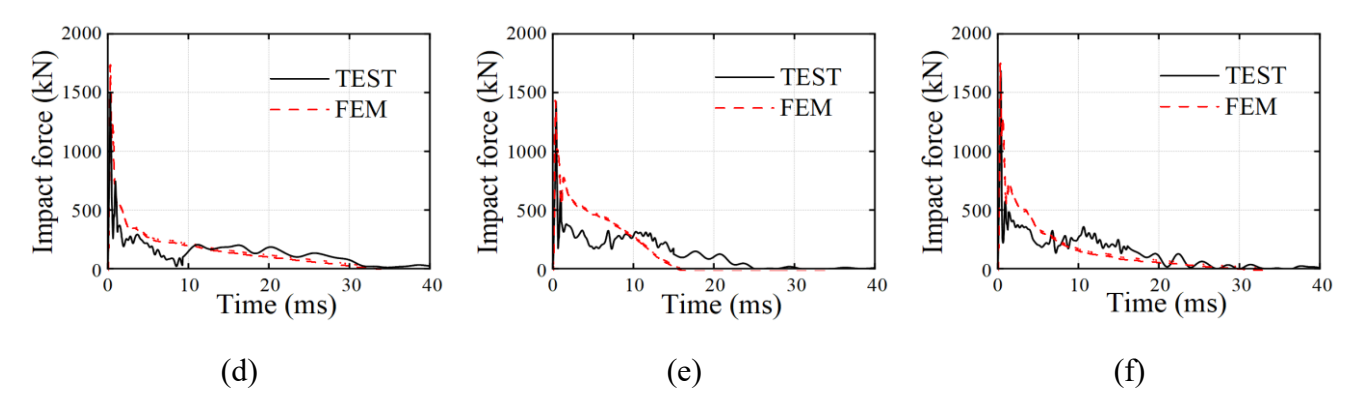


Fig. 24. Impact force time history curves by test and numerical simulation: (a) H1.8-1/2-1.5; (b)

H1.8-1/3-1.5; (c) L1.8-1/2-1.5; (d) L1.8-1/2-2.0; (e) H1.2-1/2-1.5; and (f) H1.2-1/2-2.0.

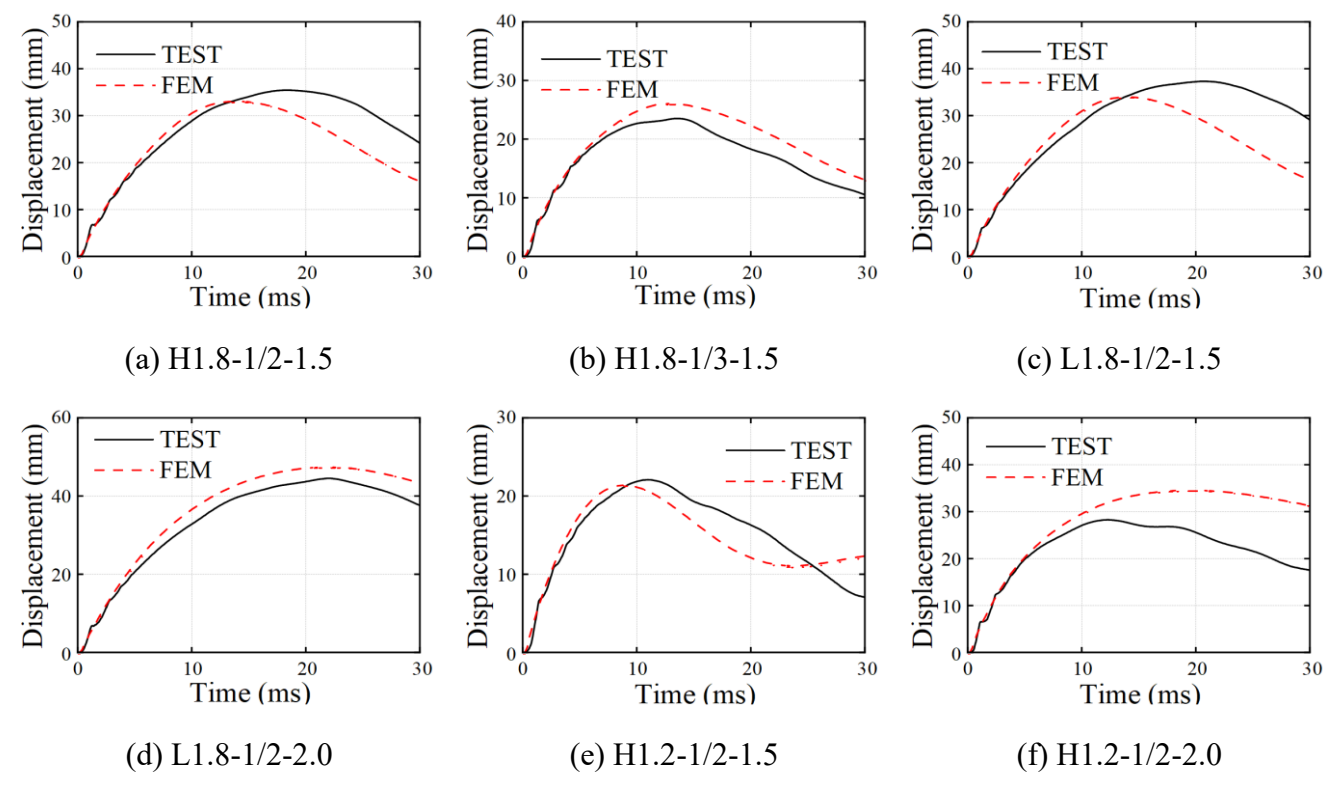


Fig. 25. Displacement time history curves by test and numerical simulation: (a) H1.8-1/2-1.5; (b) H1.8-1/3-1.5; (c) L1.8-1/2-1.5; (d) L1.8-1/2-2.0; (e) H1.2-1/2-1.5; and (f) H1.2-1/2-2.0.

Parametric Analysis

In this study, all specimens were subjected to vertical loading on the loading beam via a hydraulic jack to simulate the axial pressure for engineering application, though the load slightly deviated from the uniform distribution under actual conditions. Consequently, the finite element model was modified accordingly, as shown in **Fig. 26**.

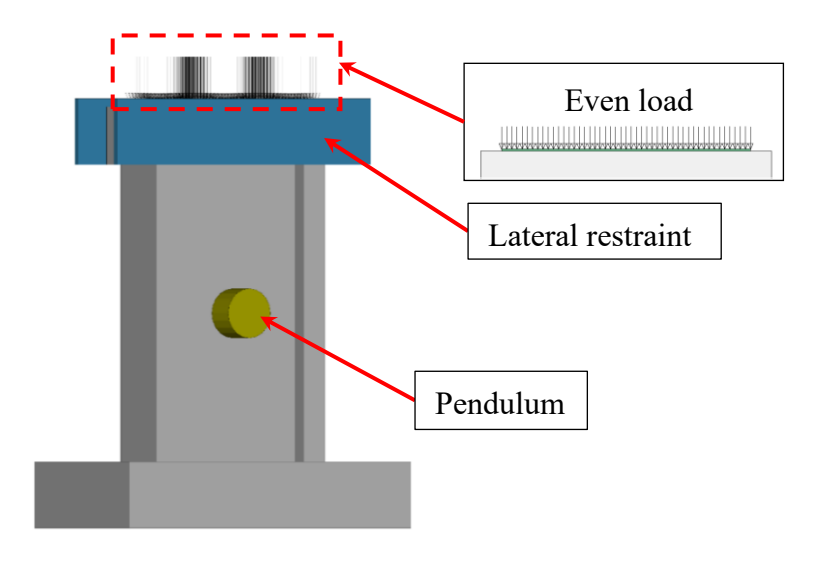


Fig. 26. Finite element analysis model of even load

The revised model does not constrain the vertical displacement at the top of the loading beam; instead, a vertical uniform load is applied. A steel plate with the same cross-sectional dimensions as the specimen is placed above the loading beam to transmit the uniform load and prevent local failure, while other boundary conditions remain unchanged.

Effect of axial compression ratio

Considering safety, the axial compression ratio of all specimens in this test was set as 0.024. Finite element analysis was conducted to investigate the impact resistance of RC shear walls under varying axial compression ratios (n = 0.1, 0.2, 0.3, 0.4, 0.5).

Fig. 27 and Fig. 28 show the impact force and displacement time history curves for different n values, respectively. Compared with n = 0.1, increasing n to 0.2, 0.3, 0.4, and 0.5 resulted in a 2.7%, 4.6%, 5.7%, and 5.8% increment in peak impact force, respectively, and a 24.3%, 35.7%, 40.1%, and 36.2% decrease in peak displacement. The axial compression ratio significantly affected peak displacement, while causing a relatively minor effect on peak force. The increased axial pressure primarily enhanced global specimen stiffness other than the local stiffness. However, this stiffening effect and its influence on peak displacement gradually weakened with further increases in axial compression ratio. Fig. 29 shows the failure modes of RC shear walls under different axial compression ratios. At an axial compression ratio of 0.3, severe concrete failure was observed on the backside of the impact area. As the ratio increased to 0.4 and 0.5, severe compressive-flexural failure occurred within 5 ms after reaching peak displacement, accompanied by extensive concrete failure in the impact area. It is due to the significant reduction in the specimen's global flexural stiffness caused by

wall deformation under impact loading, which accelerated crack propagation, ultimately leading to component failure.

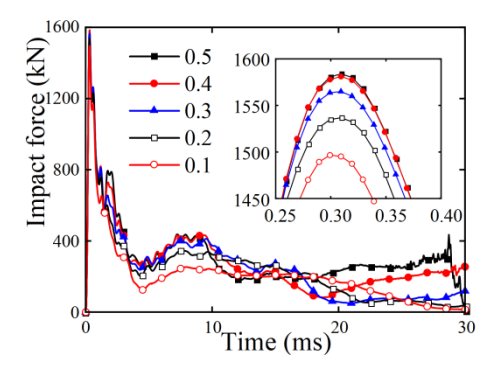


Fig. 27. Impact force time history curves of specimens under different axial compression ratios

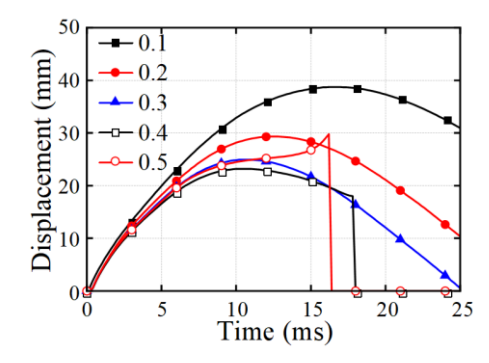
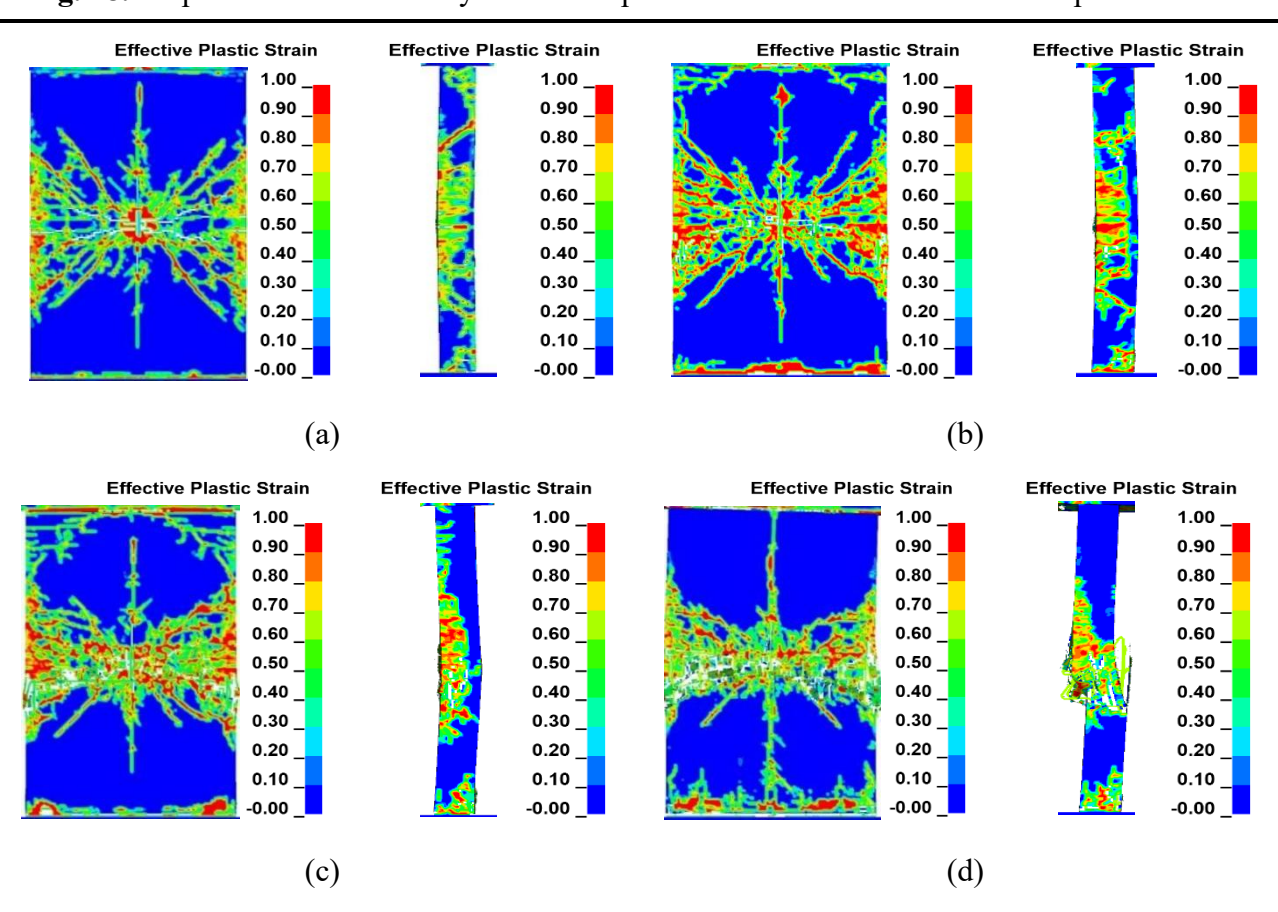


Fig. 28. Displacement time history curves of specimens under different axial compression ratios



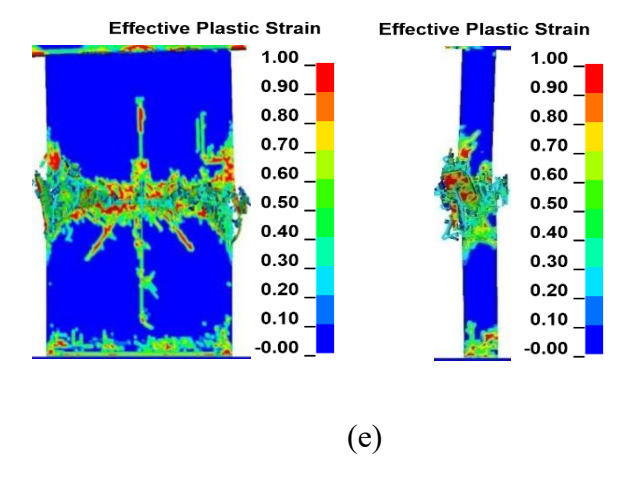
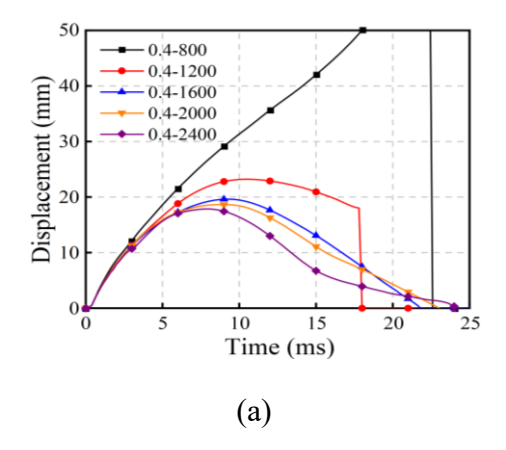


Fig. 29. Failure modes of specimens under different axial compression ratio: (a) n=0.1; (b) n=0.2; (c) n=0.3; (d) n=0.4; and (e) n=0.5.

Effect of wall width

Due to the spatial limitations of the testing site, the effect of wall width on impact resistance was not considered in the experiment; therefore, numerical simulations were used to complement the investigation of this parameter. Numerical models of RC shear walls with widths of 800 mm, 1200 mm, 1600 mm, 2000 mm were analyzed, with specimens labeled as "n-width" (e.g., 0.4-800 denotes n=0.4 and width=800 mm).



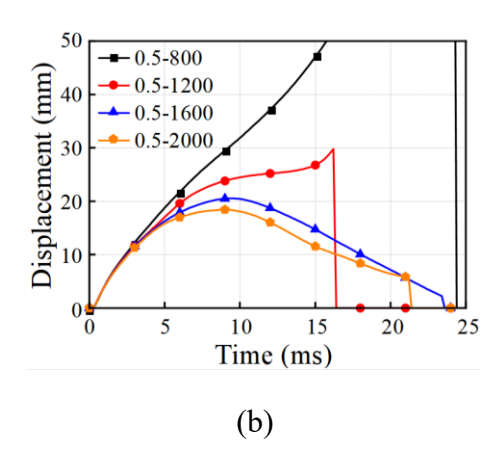
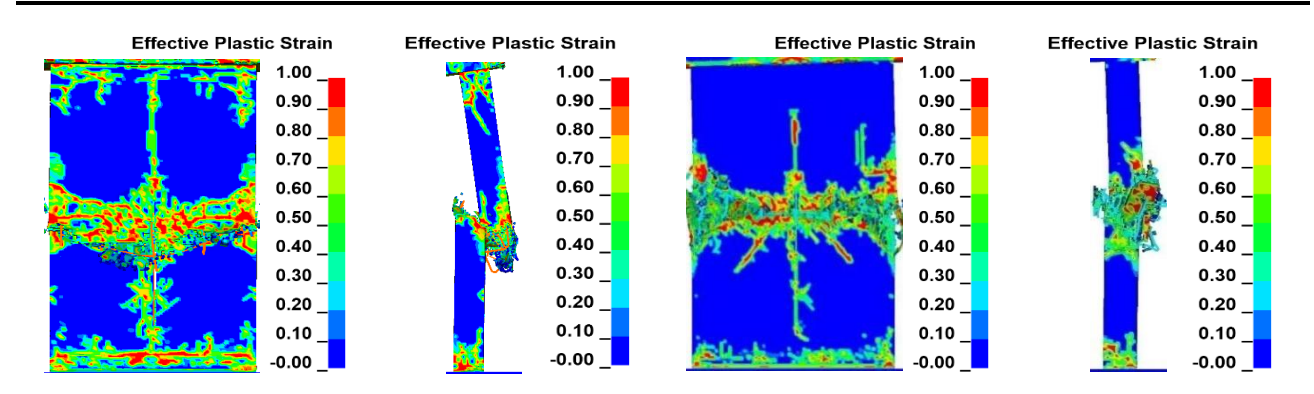


Fig. 30. Displacement time history curves of specimens: (a) n=0.4 series; and (b) n=0.5 series.



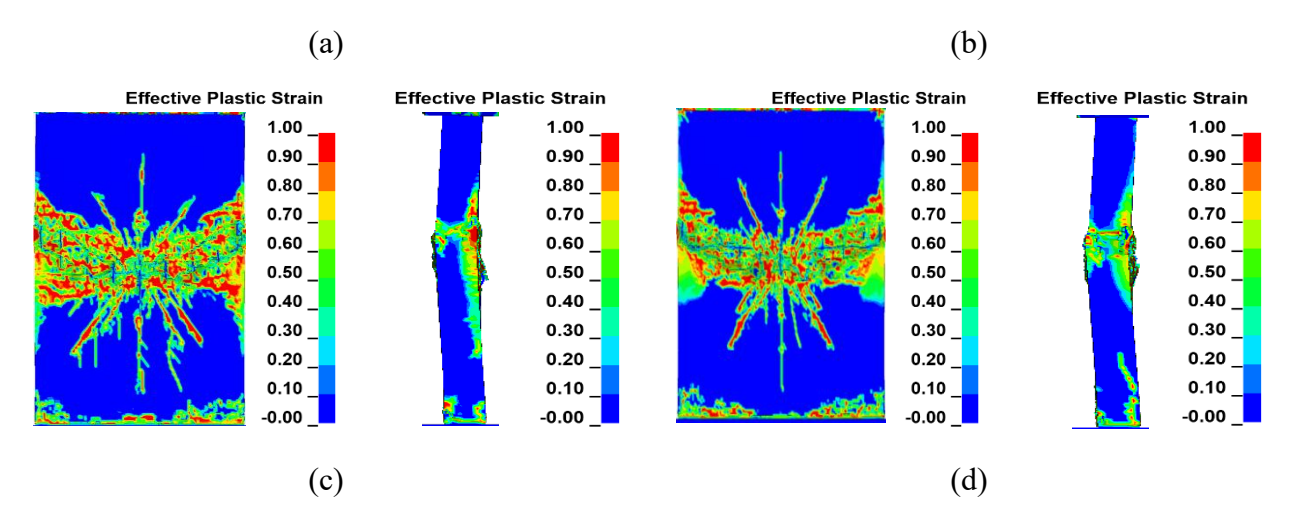


Fig. 31. Failure modes of RC shear walls: (a) 0.5-800; (b) 0.5-1200; (c) 0.5-1600; and (d) 0.5-2000.

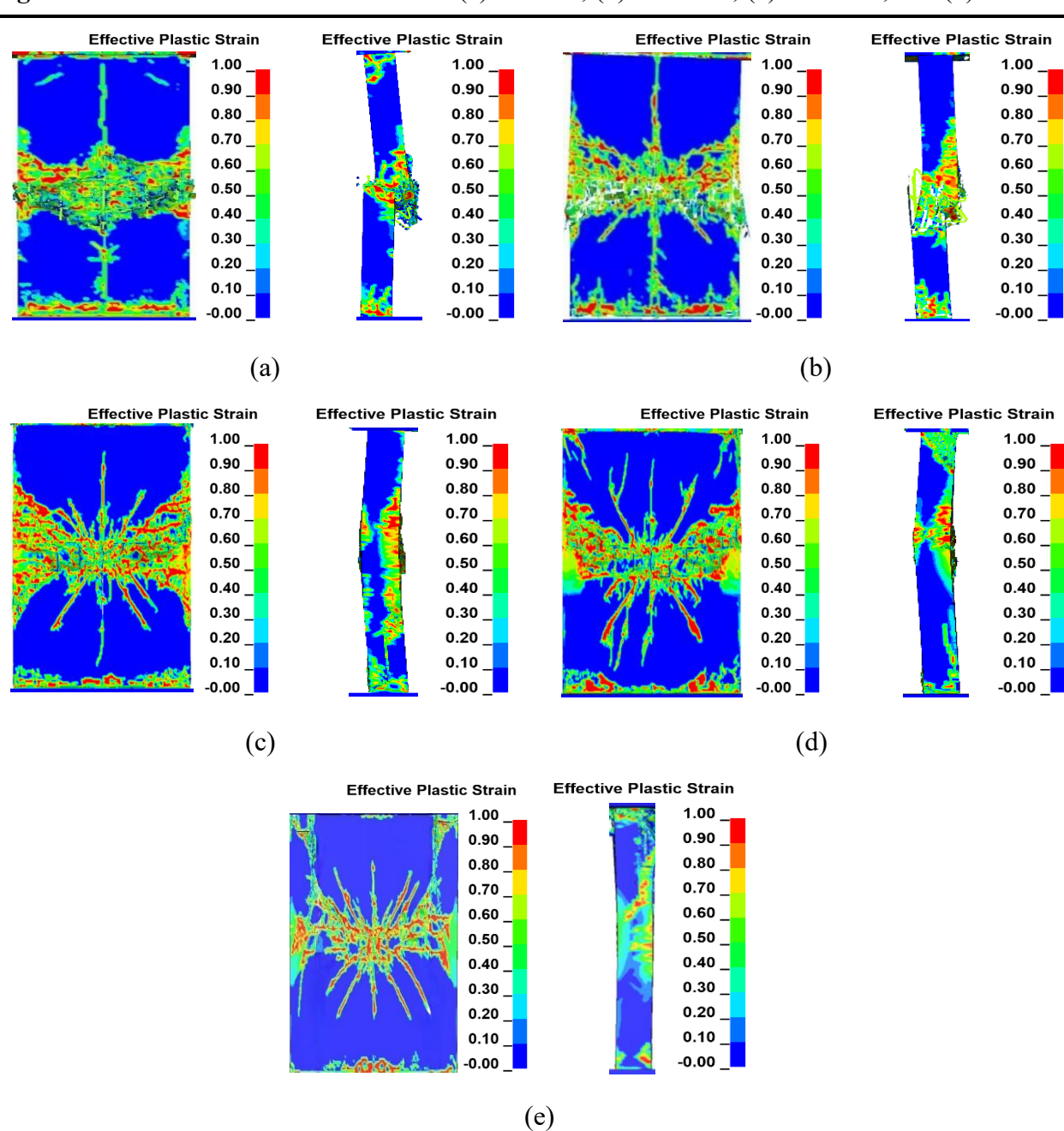


Fig. 32. Failure modes of RC shear walls: (a) 0.4-800; (b) 0.4-1200; (c) 0.4-1600; (d) 0.4-2000; and

Fig. 30 compares displacement time history curves, showing that the 800 mm width specimen suffered compressive-flexural failure due to significantly reduced flexural rigidity, with severe impact zone damage precluding accurate measurement of the peak displacement. For the same axial compression ratio, all specimens reached peak displacement at similar times: peak displacements for 0.4-1200 to 0.4-2000 were 23.2 mm, 19.6 mm, and 18.6 mm, respectively, while those for 0.5-1200 to 0.5-2000 were 24.7 mm, 20.5 mm, and 18.4 mm. Results indicate that increasing wall width reduces peak displacement, though the effect diminishes as wall width continues to increase. To validate this pattern, consider the wall specimen labeled 0.4-2400 (axial compression ratio: 0.4) as an example. As shown in Fig. 30. Displacement time history curves of specimens: (a) n=0.4 series; and (b) n=0.5 series., this specimen exhibits a peak displacement of 17.7 ms. These results confirm that increasing wall width reduces peak displacement, though this effect diminishes progressively with further width enlargement.

Fig. 31-

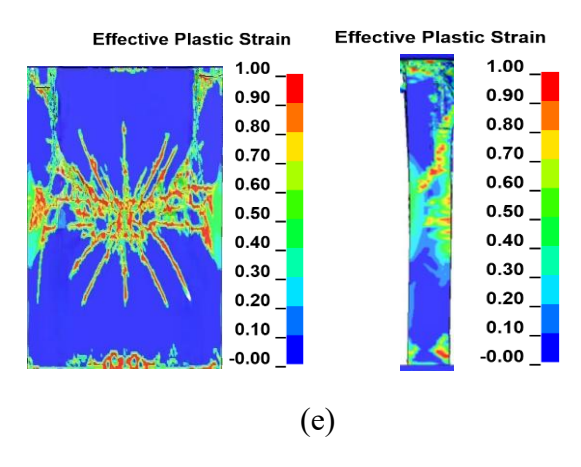


Fig. 32

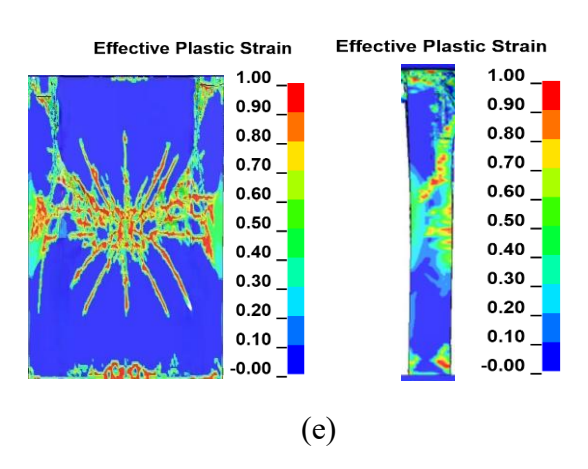


Fig. 32 show failure modes, revealing that the wider walls exhibit higher flexural rigidity, secondary damage remains inevitable in RC shear walls under high axial compression ratios after impact loading.

Effect of impact energy

Due to the challenge of quantifying impact energy in the test, finite element analysis was used to investigate the dynamic response of RC shear walls under varying impact masses and velocities. RC shear walls do not exhibit pure bending or shear failure modes under impact loading. To quantify these failure modes, the displacement difference Δ between the impact point and edge position is defined to characterize the severity of local deformation relative to global deformation: a smaller Δ indicates a higher propensity for bending failure, while a larger Δ suggests a greater tendency toward shear failure. As shown in Fig. 33, the peak displacement at impact point D1 characterizes the specimen's local deformation, and the displacement at edge position D2 when D1 reaches its peak represents the global deformation.

Fig. 34 shows the relationship between the displacement difference Δ of all specimens and impact mass/velocity. In the specimen label 1.5-1, "1.5" denotes an impact mass of 1.5 t, and "1" denotes an impact velocity of 1 m/s. Fig. 34. Displacement difference of specimens: (a) impact mass; and (b) impact velocity. show that Δ increases significantly with impact velocity at constant mass, while Δ grows more gradually with mass at constant velocity—particularly, mass has no obvious effect on Δ at low velocities. This suggests that impact velocity has a more significant influence on Δ than mass. Notably, Δ increases with impact energy below 16,000 J, which can be treated as a threshold: Δ drops sharply above this value. For example, the displacement difference Δ values of specimens 2.0-4 and 1.5-5 are 9.3 mm and 9.2 mm, respectively, while those of specimens 2.5-4 and 2.0-5 are 7.6 mm and 4.0 mm, respectively. According to this pattern, the displacement difference Δ of N-2.5-5 is smaller than that of N-2.0-5. However, the measured Δ value of N-2.5-5 is larger, which is attributed to the fact that the higher impact mass causes large local deformation in the specimen, potentially leading to a temporary increase in Δ .

To further validate the hypothesis, **Fig. 35** compares the peak displacement variations of measuring points D1 and D2. In the specimen label DI-1.5-1, "DI" denotes the peak displacement at impact point D1, while "D-1.5-1" indicates the peak displacement of D2 when D1 reaches its peak. where, "1.5" represents an impact mass of 1.5 tons, and "1" denotes an impact velocity of 1 m/s. When the impact energy exceeds 16,000 J, the slope of D-2.0-X exceeds that of DI-2.0-X, and D-X-

5 has a steeper slope than DI-X-5, see in **Fig. 35**. It indicates that at lower impact energies, specimens resist loads primarily through local deformation, whereas at higher energies, the impact load exceeds the global flexural capacity, causing overall flexural failure.

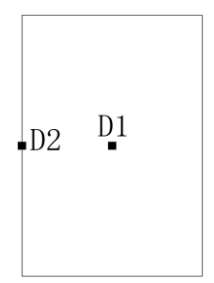
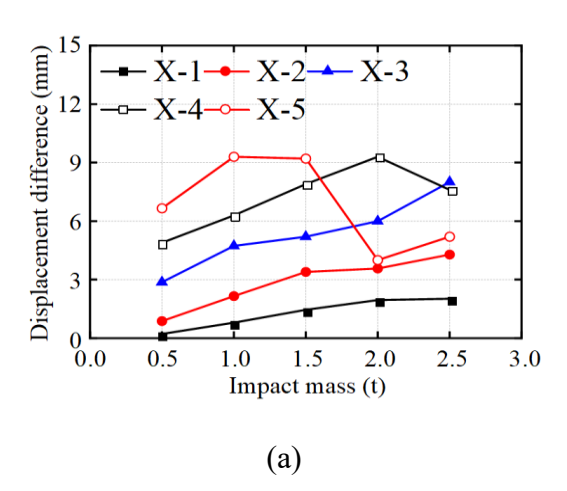


Fig. 33. Distribution diagram of displacement measuring point of specimen



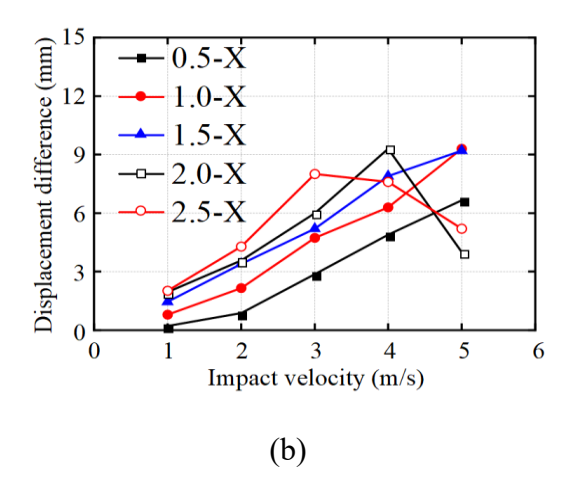
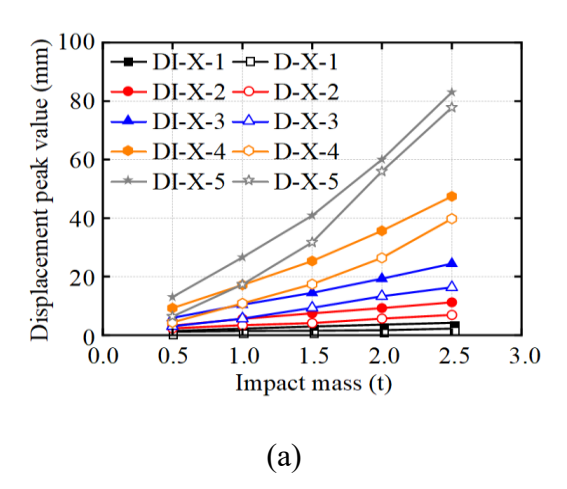


Fig. 34. Displacement difference of specimens: (a) impact mass; and (b) impact velocity.





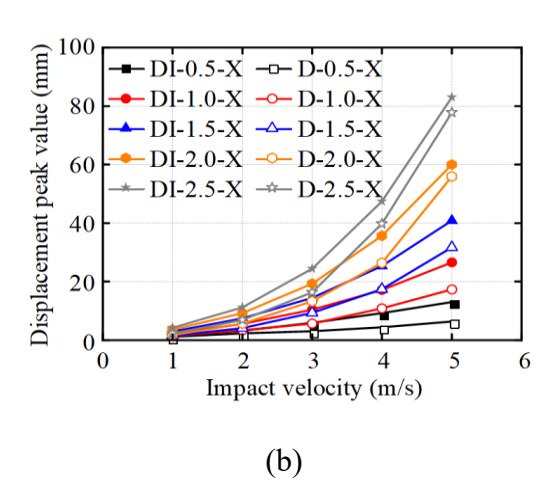


Fig. 35. Peak displacement diagram of specimens: (a) impact mass; and (b) impact velocity.

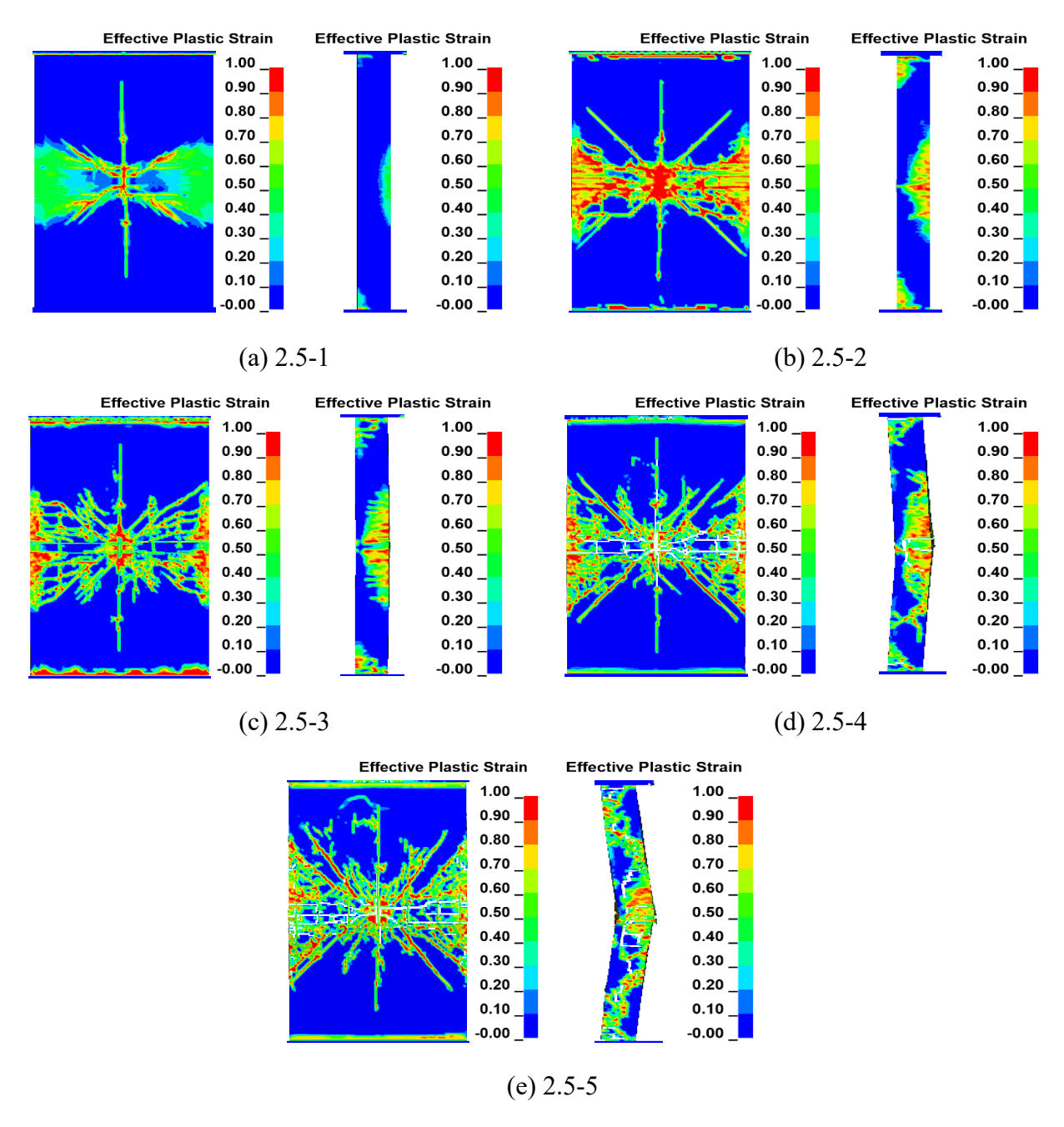


Fig. 36. Failure mode of specimens: (a) 2.5-1; (b) 2.5-2; (c) 2.5-3; (d) 2.5-4; and (e) 2.5-5

Fig. 36shows the failure modes of 2.5-X series specimens. At an impact velocity of 4 m/s (impact energy exceeding 16,000 J), the specimen sides exhibit obvious bending failure characteristics compared to 3 m/s, with severe deformation in the horizontal cross-section at the impact point.

Analytical Model for displacement

The peak displacement is one of the most important indexes to evaluate the impact resistance of components. Some scholars have derived the displacement-based analytical model according to the basic principles of energy and momentum (Yang, Y., Lam, N. T. K., and Zhang, L. 2012. Evaluation of simplified methods of estimating beam responses to impact. *International Journal of Structural Stability and*

Dynamics, 12(03), 1250016.; Lam, N. T. K., Yong, A. C. Y., Lam, C., Kwan, J. S., Perera, J. S., Disfani, M. M., and Gad, E. 2018. Displacement-based approach for the assessment of overturning stability of rectangular rigid barriers subjected to point impact. *Journal of Engineering Mechanics*, 144(2), 04017161.) to predict the performance of components under impact load.

Generally, the assumption of identical transmission of kinetic energy was adopted model mentioned above. This approach relies on the ideal elastic state, which ignores energy loss from the impactor rebounding after impact. However, in reality, the kinetic energy of impactor can not be fully transferred to the component. So, the model has been modified based on energy partitioning and formularized as Eqs. (1) using momentum conservation before and after collision between the impactor and impacted component. Lam et al. (Lam, N. T. K., Yong, A. C. Y., Lam, C., Kwan, J. S., Perera, J. S., Disfani, M. M., and Gad, E. 2018. Displacement-based approach for the assessment of overturning stability of rectangular rigid barriers subjected to point impact. *Journal of Engineering Mechanics*, 144(2), 04017161.) further introduced the coefficient of restitution (COR), defined as the ratio of post- to pre-impact velocities, as shown in Eq. (3), by assuming that the impactor does not embed in the component.

$$mv_0 = m_1 v_2 - mv_1 \tag{1}$$

$$\lambda = \frac{m_1}{m} \tag{2}$$

$$COR = \frac{v_1 + v_2}{v_0}$$
 (3)

$$\frac{KE_2}{KE_0} = \frac{\frac{1}{2}m_1(v_2)^2}{\frac{1}{2}m(v_0)^2} = \lambda \left(\frac{1+COR}{1+\lambda}\right)^2$$
 (4)

$$\Delta = \frac{mv_0}{\sqrt{km}} \sqrt{\lambda \left(\frac{1+COR}{1+\lambda}\right)^2}$$
 (5)

where m represent the impactor mass; v_0 is impactor initial velocity m_1 denotes the effective mass of the impacted component; v_1 represents the post-impact velocity of the impactor; v_2 is the velocity of the component during impact; λ is the ratio of the effective mass of the impacted component to the mass of the impactor; kE_0 is the initial kinetic energy of the impactor and kE_2 is the kinetic energy imposed onto the target immediately following the impact.

This model is only applicable to components that remain in the elastic stage without plastic deformation after suffering impact loads. However, when the component undergoes the large impact

energy, it will exceed the yield limit state, so the model has certain limitations. Ali (Ali, M., Sun, J., Lam, 526 N., Zhang, L., and Gad, E. 2014. Simple hand calculation method for estimating deflection generated by the low 527 velocity impact of a solid object. Australian Journal of Structural Engineering, 15(3), 243-259.) made the 528 corresponding modifications to the model: an elastoplastic model has been proposed by simplifying 529 the nonlinear force-displacement curve in terms of the principle of energy conservation: 530

$$\frac{mv_0^2}{2} \left(\lambda \left(\frac{1 + COR}{1 + \lambda} \right)^2 \right) = \frac{F_y \Delta_y}{2} + F_y \left(\Delta_m - \Delta_y \right)$$
 (6)

$$\Delta_m = \frac{mv_0^2}{2F_y} \left(\lambda \left(\frac{1 + COR}{1 + \lambda} \right)^2 \right) + \frac{\Delta_y}{2}$$
 (7)

where F_y is yield load. Δ_y represents displacement of the impacted component at yield. Δ_m is 533

final displacement of the impacted component.

534

535

536

537

538

543

544

545

A simplified calculation method is used to calculate the bending stiffness of reinforced concrete members. Eqs. (8)-(11) are derived by Priestley et al. (Powell, G. H. 2008. Displacement-based seismic design of structures. Earthquake spectra, 24(2), 555-557.) based on the bending moment-curvature analysis of axially loaded structures.

$$k_{eff} = \frac{4*48EI_{eff}}{h^3} \tag{8}$$

$$M_{v} = \phi M_{u} = 0.8 A_{st} f_{v} (0.9d) \tag{9}$$

$$\phi_{y} = \frac{1.7\varepsilon_{sy}}{D} \tag{10}$$

$$EI_{eff} = \frac{M_y}{\phi_y} \tag{11}$$

where $\textit{k}_{\textit{eff}}$ represents the generalized stiffness; E is Young's modulus; $\textit{I}_{\textit{eff}}$ refers to the section moment of inertia; h represents the component height; M_y is the yield moment; M_u is the ultimate moment; A_{st} is the area of tension steel; ϕ_v is the yield curvature; ε_{sv} refers to the yield strain of steel; and D represents the component thickness. 546

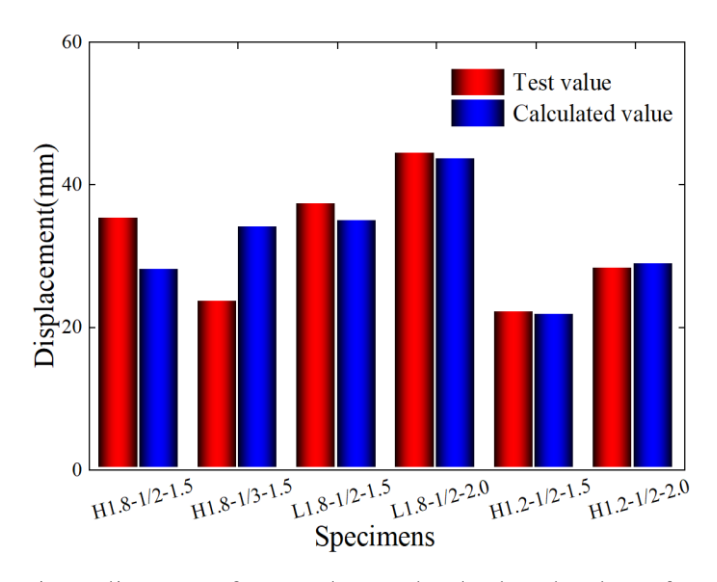


Fig. 37. Comparison diagram of test value and calculated value of peak displacement

Fig. 37 shows the comparison between the test and calculated values of the peak displacements of all specimens. The experimental peak displacement agrees reasonably well with the calculated values, with errors within the range of 10%. Consequently, the energy-based D-B model can effectively predict the maximum displacement of RC shear wall under impact load.

Conclusions

Based on the pendulum impact test and numerical parametric analysis, the following key conclusions can be made:

- (1) When subjected to impact loads, RC shear walls exhibit two failure modes: punching shear failure (concrete near the impact point cracks annularly and propagates radially) and bending failure (horizontal flexural cracks develop in the mid-span region).
- (2) Reducing wall height and impact position improves bending stiffness. This reduces the mid-span peak displacement and shortens both the overall impact force response time and the process of reaching peak displacement. Increasing the reinforcement ratio enhances the overall stiffness and peak impact force, but not significantly, while reducing the overall impact force response time and mid-span peak displacement. With the increase of drop height, the peak value of impact force, mid-span displacement peak, and the time required to reach displacement peak increase significantly.
- (3) When impact energy is constant, the energy absorption capacity of the specimen is primarily governed by its overall stiffness. Higher overall stiffness correlates with lower energy absorption capacity. The energy-based D-B model effectively predicts the maximum displacement of RC shear walls under impact load, which can be used to assess their deformation.

- 569 (4) Finite element parameter analysis shows that increasing the axial compression ratio enhances
- specimen overall stiffness and significantly reduces mid-span peak displacement of RC shear
- walls, though this effect diminishes with higher axial compression ratios. Increasing wall width
- significantly improves flexural stiffness and reduces impact-induced mid-wall displacement; but
- it cannot effectively prevent bending failure under vertical loads. Compared with the impact
- mass, the impact velocity has a more significant effect on the displacement difference Δ .

575 Data Availability Statement

- The data used to support the findings of this study are available from the corresponding author upon
- 577 request.
- 578 Conflicts of Interest
- The authors declare no potential conflicts of interest with respect to the research, authorship, and/or
- 580 publication of this article.
- 581 Acknowledgement
- The first author would like to acknowledge the financial support provided by the National Natural
- Science Foundation of China (grant No. 51968013), The Guangxi Natural Science Foundation (Grant
- 584 No., 2022GXNSFAA035529)

References

585

595 596

597 598

599 600

601

602

608

- ACI (American Concrete Institute). 2014. *Building code requirements for structural concrete (ACI 318-14) and commentary (318R-14)*. ACI 318. Farmington Hills, MI: ACI.
- Adhikary, S. D., Li, B., and Fujikake, K. 2015. Residual resistance of impact-damaged reinforced concrete beams. *Magazine of Concrete Research*, 67(7), 364-378.
- Ali, M., Sun, J., Lam, N., Zhang, L., and Gad, E. 2014. Simple hand calculation method for estimating deflection generated by the low velocity impact of a solid object. *Australian Journal of Structural Engineering*, *15*(3), 243-259.
- Astaneh-Asl, A. 2002. Seismic behavior and design of composite steel plate shear walls. Moraga, CA, USA:
 Structural Steel Educational Council.
 - Bhatti, A. Q., Kishi, N., and Tan, K. H. 2011. Impact resistant behaviour of RC slab strengthened with FRP sheet. *Materials and structures*, 44, 1855-1864.
 - Consolazio, G. R., and Cowan, D. R. 2005. Numerically efficient dynamic analysis of barge collisions with bridge piers. *Journal of Structural Engineering*, 131(8), 1256-1266.
 - Consolazio, G. R., and Davidson, M. T. 2008. Simplified dynamic analysis of barge collision for bridge design. *Transportation Research Record*, 2050(1), 13-25.
 - Do, T. V., Pham, T. M., and Hao, H. 2019. Impact force profile and failure classification of reinforced concrete bridge columns against vehicle impact. *Engineering Structures*, *183*, 443-458.
- Fan, W., Liu, Y., Liu, B., and Guo, W. 2016. Dynamic ship-impact load on bridge structures emphasizing shock spectrum approximation. *Journal of Bridge Engineering*, 21(10), 04016057.
- Fu, F. 2013. Dynamic response and robustness of tall buildings under blast loading. *Journal of Constructional steel* research, 80, 299-307.
 Fuilkake, K. 2014. Impact performance of ultra-high-performance fiber reinforced concrete beam and its analytical
 - Fujikake, K. 2014. Impact performance of ultra-high-performance fiber reinforced concrete beam and its analytical evaluation. *International Journal of Protective Structures*, *5*(2), 167-186.
 - Fujikake, K., Li, B., and Soeun, S. 2009. Impact response of reinforced concrete beam and its analytical evaluation. *Journal of Structural Engineering*, *135*(8), 938-950.
- Gesund, H., and Kaushik, Y. P. 1970. Yield line analysis of punching failures in slabs. *International Association for Bridges and Structural Engineering*, 30(1), 41-60.
- 613 Gholipour, M., and Alinia, M. M. 2016. Behavior of multi-story code-designed steel plate shear wall structures regarding bay width. *Journal of Constructional Steel Research*, *122*, 40-56.
- Goswami, A., Adhikary, S. D., and Li, B. 2019. Predicting the punching shear failure of concrete slabs under low velocity impact loading. *Engineering Structures*, *184*, 37-51.
- 617 Guner, S., and Vecchio, F. J. 2012. Simplified method for nonlinear dynamic analysis of shear-critical frames. ACI

618 *Structural Journal*, 109(5), 727.

627

628

629

630

631 632

635

636 637

638

639 640

641

642

643

644 645

646

647

648 649

652 653

654

655 656

657

658

659 660

661

662

663

664 665

666

667

- Guo, J., Cai, J., and Chen, W. 2017. Inertial effect on RC beam subjected to impact loads. *International Journal of Structural Stability and Dynamics*, 17(04), 1750053.
- Hallquist, J. O. 2007. LS-DYNA–Keyword user's manual, version 971, livermore soft. California, USA: Technology
 Corporation (LSTC).
- Kandil, K. S., Nemir, M. T., Ellobody, E. A., and Shahin, R. I. 2014. Strain Rate Effect on the Response of Blast Loaded Reinforced Concrete Slabs. *World Journal of Engineering and Technology*, 2(04), 260.
- Kumar, V., Iqbal, M. A., and Mittal, A. K. 2018. Experimental investigation of prestressed and reinforced concrete plates under falling weight impactor. *Thin-Walled Structures*, *126*, 106-116.
 - Lam, N. T. K., Yong, A. C. Y., Lam, C., Kwan, J. S., Perera, J. S., Disfani, M. M., and Gad, E. 2018. Displacement-based approach for the assessment of overturning stability of rectangular rigid barriers subjected to point impact. *Journal of Engineering Mechanics*, 144(2), 04017161.
 - Lan, Y., Zhang, R., Jin, L., and Du, X. 2023. Impact performance of BFRP and steel-reinforced concrete beams with different span-to-depth ratios: Numerical and analytical studies. *Science China Technological Sciences*, 66(2), 301-319.
- Lefas, I. D., Kotsovos, M. D., and Ambraseys, N. N. 1990. Behavior of reinforced concrete structural walls: strength,
 deformation characteristics, and failure mechanism. *Structural Journal*, 87(1), 23-31.
 - Li, H., Chen, W., and Hao, H. 2020. Factors influencing impact force profile and measurement accuracy in drop weight impact tests. *International Journal of Impact Engineering*, 145, 103688.
 - Li, H., Chen, W., Pham, T. M., and Hao, H. 2021. Analytical and numerical studies on impact force profile of RC beam under drop weight impact. *International Journal of Impact Engineering*, *147*, 103743.
 - Massone, L. M., Sayre, B. L., and Wallace, J. W. 2017. Load–Deformation responses of slender structural steel reinforced concrete walls. *Engineering Structures*, *140*, 77-88.
 - Murray, Y. D. 2007. *Users manual for LS-DYNA concrete material model 159*. United States: Federal Highway Administration
 - Othman, H., and Marzouk, H. 2016. An experimental investigation on the effect of steel reinforcement on impact response of reinforced concrete plates. *International Journal of Impact Engineering*, 88, 12-21.
 - Pham, A. T., Tan, K. H., and Yu, J. 2017. Numerical investigations on static and dynamic responses of reinforced concrete sub-assemblages under progressive collapse. *Engineering Structures*, 149, 2-20.
 - Powell, G. H. 2008. Displacement-based seismic design of structures. Earthquake spectra, 24(2), 555-557.
 - Qu, H., Huo, J., Xu, C., and Fu, F. 2014. Numerical studies on dynamic behavior of tubular T-joint subjected to impact loading. *International Journal of Impact Engineering*, 67, 12-26.
- Ross, T. J., and Krawinkler, H. 1985. Impulsive direct shear failure in RC slabs. *Journal of Structural Engineering*, 111(8), 1661-1677.
 - Said, A. M. I., and Mouwainea, E. M. 2022. Experimental investigation on reinforced concrete slabs under high-mass low velocity repeated impact loads. *Structures*, *35*, 314-324.
 - Sharma, H., Gardoni, P., and Hurlebaus, S. 2015. Performance-based probabilistic capacity models and fragility estimates for RC columns subject to vehicle collision. *Computer-Aided Civil and Infrastructure Engineering*, 30(7), 555-569.
 - Sohel, K. M. A., Al-Jabri, K., and Al Abri, A. H. S. 2020. Behavior and design of reinforced concrete building columns subjected to low-velocity car impact. *Structures*, 26, 601-616.
 - Soltani, H., Khaloo, A., and Sadraie, H. 2020. Dynamic performance enhancement of RC slabs by steel fibers vs. externally bonded GFRP sheets under impact loading. *Engineering Structures*, 213, 110539.
 - Tai, Y. S., Chu, T. L., Hu, H. T., and Wu, J. Y. 2011. Dynamic response of a reinforced concrete slab subjected to air blast load. *Theoretical and applied fracture mechanics*, 56(3), 140-147.
 - Tsang, H. H., and Lam, N. T. 2008. Collapse of reinforced concrete column by vehicle impact. *Computer-Aided Civil and Infrastructure Engineering*, 23(6), 427-436.
 - Wang, R., Han, L. H., and Hou, C. C. 2013. Behavior of concrete filled steel tubular (CFST) members under lateral impact: Experiment and FEA model. *Journal of Constructional Steel Research*, 80, 188-201.
 - Wang, W., and Morgenthal, G. 2017. Dynamic analyses of square RC pier column subjected to barge impact using efficient models. *Engineering Structures*, *151*, 20-32.
- Wang, W., Zhou, R.X. and Zhong, J. 2022. Efficient numerical analyses of RC beams subjected to impact loading using axial-flexure-shear fiber beam model. *Structures*, *41*, 1559-1569.
- Wu, Y., Crawford, J. E., and Magallanes, J. M. 2012. Performance of LS-DYNA concrete constitutive models. *12th International LS-DYNA users conference*, 1, 1-14.
- Xu, B., and Zeng, X. 2014. Experimental study on the behaviors of reinforced concrete beams under impact loadings.
 China Civil Engineering Journal, 47(2), 41-51. (in chinese)
- Yang, Y., Lam, N. T. K., and Zhang, L. 2012. Evaluation of simplified methods of estimating beam responses to impact. *International Journal of Structural Stability and Dynamics*, *12*(03), 1250016.
- Yong, A. C. Y., Lam, N. T. K., Menegon, S. J., and Gad, E. F. 2020a. Cantilevered RC wall subjected to combined

static and impact actions. *International Journal of Impact Engineering*, 143, 103596.

- Yong, A. C. Y., Lam, N. T. K., Menegon, S. J., and Gad, E. F. 2020b. Experimental and analytical assessment of flexural behavior of cantilevered RC walls subjected to impact actions. *Journal of Structural Engineering*, 146(4), 04020034.
- Zhang, X., Hao, H., and Li, C. 2016. Experimental investigation of the response of precast segmental columns subjected to impact loading. *International Journal of Impact Engineering*, *95*, 105-124.
 - Zhao, Q., and Astaneh-Asl, A. 2004. Cyclic behavior of traditional and innovative composite shear walls. *Journal of Structural Engineering*, 130(2), 271-284.
 - Zhou, Y., Zhang, X., Yi, F., Sun, J. M., Ni, J., Li, T., and Yi, W. J. 2024. Impact resistance and performance of precast shear walls with various connections under axial and lateral loads. Engineering Structures, 318, 118748.
 - Zineddin, M. 2008. Simulation of reinforced concrete slab behavior under impact loading. AEI 2008: Building Integration Solutions, 1-9.
 - Zineddin, M., and Krauthammer, T. 2007. Dynamic response and behavior of reinforced concrete slabs under impact loading. *International Journal of Impact Engineering*, *34*(9), 1517-1534.